The Microphysical Structure and Evolution of Hawaiian Rainband Clouds. Part III: A Test of the Ultragiant Nuclei Hypothesis

MARCIN J. SZUMOWSKI

Department of Atmospheric Sciences, University of Illinois, Urbana–Champaign, Urbana, Illinois, and Illinois State Water Survey, Champaign, Illinois

ROBERT M. RAUBER

Department of Atmospheric Sciences, University of Illinois, Urbana–Champaign, Urbana, Illinois

HARRY T. OCHS III

Illinois State Water Survey, Champaign, Illinois, and Department of Atmospheric Sciences, University of Illinois, Urbana–Champaign, Urbana, Illinois

(Manuscript received 10 April 1998, in final form 17 September 1998)

ABSTRACT

A Lagrangian drop-growth trajectory model, applied within dual-Doppler-derived four-dimensional kinematic fields, is used to test the hypothesis that accretion of cloud water on giant and ultragiant cloud condensation nuclei (CCN) can explain the growth of raindrops in warm maritime convective clouds. Radar data collected within offshore rainbands during the 1990 Hawaiian Rainband Project are used to provide realistic timescales and magnitudes of convective updrafts and to capture the horizontal flow variations responsible for transporting drops into and out of these updrafts. The range of conditions under which cloud droplets can grow to large raindrops during simple up–down trajectories is determined.

The model results show that accretion of cloud water on giant and ultragiant nuclei can account for the formation of rain in observed timescales. Raindrops with diameters of 1–4 mm formed for the entire range of tested conditions. Maximum drop sizes ranged from 3.5 to 8.5 mm. The general tendency in the simulations was for the largest drops to fall within regions of radar reflectivity greater than 35 dB*Z*, and for the smaller drops to fall in parts of the rainband with weaker reflectivity. In the control runs, which the authors believe represent natural conditions, drops as large as 5 mm formed on cloud droplets whose initial diameters were comparable to deliquesced sea salt particles observed in concentrations of $\sim$10 to 10^3 m^{-3} near the base of Hawaiian clouds. The growth rates and trajectories of 1–5-mm raindrops in these runs agreed well with the observed evolution of the reflectivity fields. The most rapid rate of drop growth in the model occurred during a near-suspension period and early fall through the upper parts of the cloud, which is in good agreement with the sharp reflectivity gradients observed near cloud top by the radars. Despite the time and space constraints placed on the results by the evolution of the updrafts, the calculations showed that the process of rain formation in warm maritime convective clouds is simple and efficient, provided that giant and ultragiant CCN are present near cloud base. While more complex processes leading to drop spectra broadening, such as mixing, stochastic condensation, stochastic coalescence, and breakup also occur in nature, they appear to be unnecessary to explain the rapid formation of rain in these warm maritime convective clouds.

1. Introduction

Understanding the physical processes governing the formation of rain in warm and warm-based cloud systems is essential to improve remote sensing and prediction of rainfall and to address the effects of these clouds on radiative budgets and climate. Despite nearly a half-century of research on warm rain microphysics, the dominant mechanisms responsible for the initiation of the collision–coalescence process, the subsequent broadening of the drop spectra, and the formation of rain are still unclear (Beard and Ochs 1993). The main challenge has been to explain the formation of precipitation in timescales observed in nature. The theory of stochastic coalescence (Telford 1955; Gillespie 1972, 1975) has been applied to simulate the evolution of warm rain precipitation (e.g., Berry and Reinhardt 1974; Young 1975; Reisin et al. 1998). Robertson (1974) pointed out that the main deficiency of the early sim-

Corresponding author address: Dr. Marcin J. Szumowski, Desert Research Institute, P.O. Box 60220, Reno, NV 89506.
E-mail: mszumow@dri.edu

© 1999 American Meteorological Society

Unauthenticated | Downloaded 12/05/22 11:56 AM UTC

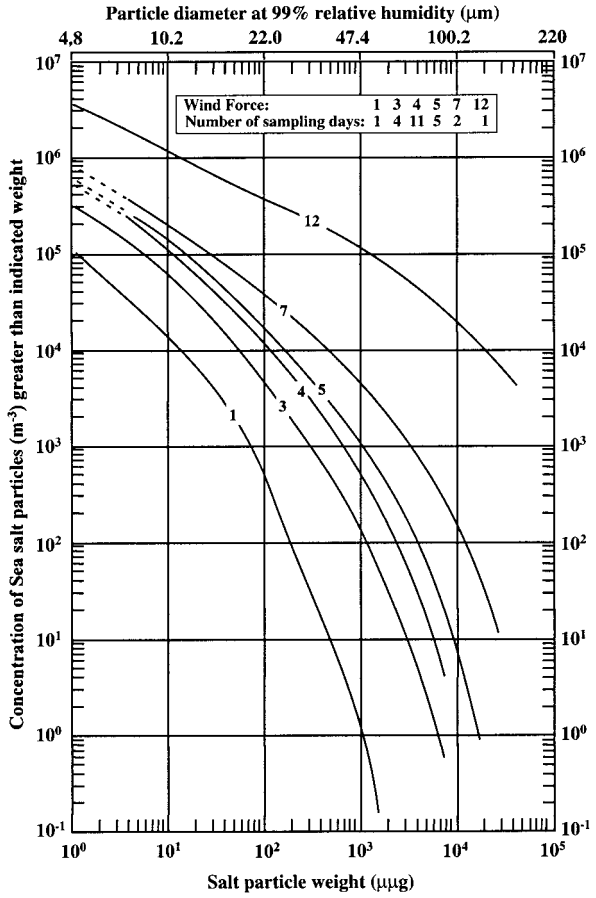

FIG. 1. Size and mass distribution of sea salt particles observed just below cloud base for different wind conditions. Curves for wind forces over the sea near Hawaii: 1 (0.5–1.5 m s^{-1}), 3 (3.5–5.0 m s^{-1}), 4 (5–8 m s^{-1}), 5 (8–10 m s^{-1}), 7 (14–17 m s^{-1}), and in a tropical storm near Florida 12 (>33 m s^{-1}) [adapted from Woodcock (1953)].

ulations, aside from inaccuracy of the numerical methods, lay in the overestimation of collection efficiencies during the early stages of drop spectra broadening. Robertson (1974) argued that using realistic collection efficiencies between small cloud droplets would greatly increase the time required for rain to form. However, Reisin et al. (1998) recently appeared to successfully simulate the evolution of a high reflectivity core in Hawaiian clouds using a fully stochastic collision–coalescence model in an idealized two-dimensional flow framework (Szumowski et al. 1998a).

An alternative, much simpler explanation of warm rain formation was first suggested by Houghton (1938) and investigated by Woodcock (1952, 1953). Woodcock (1953) measured the concentration and size distribution of salt nuclei near cloud base in marine air near Hawaii and Florida (Fig. 1). He found the concentration of giant (10^{-8} to 10^{-12} g) salt nuclei to be similar in these areas and to range from about 10^1 to 10^6 m^{-3} for typical trade wind conditions. Based on comparisons of chloride concentrations in raindrop samples of Hawaiian showers and in clear-air cloud condensation nuclei (CCN) samples, he concluded that embryonic raindrops form on giant sea salt particles and grow by collecting smaller, relatively nonsaline cloud droplets (Woodcock 1952; Woodcock and Blanchard 1955). Woodcock (1952) estimated from nuclei mass spectra and drop salinity measurements that the concentrations of raindrops in tropical convective showers are similar to the concentration of giant CCN. Woodcock and Blanchard (1955) determined that the mass of chlorine in giant sodium chloride particles in a unit volume of air was similar to the mass of chlorine in raindrops in the same volume. However, in a later study, Woodcock et al. (1971) appeared to contradict their early findings, concluding that ''in warm oceanic tradewind clouds, giant salt nuclei may not be essential to the formation of raindrops.'' They based this conclusion on data that showed that the iodine/chlorine ratio in raindrops corresponded to the ratio found in large (10^{-14} to 10^{-12} g) salt particles, but was significantly higher than that found in giant salt particles. Their data imply that raindrops in Hawaiian showers are primarily composed of cloud droplets that form on large (rather than giant) sea salt particles. This, however, is not inconsistent with the theory that a droplet that *initially triggers coalescence,* and subsequently collects thousands of smaller cloud droplets, forms on a giant salt particle.

A number of observational and modeling studies support the hypothesis that large raindrops form on giant (d_{dry} = 2 to 20 μm) and ultragiant (d_{dry} > 20 μm) CCN. Johnson (1976), Nelson and Gokhale (1968), Hindman et al. (1977a,b), and Hobbs et al. (1976, 1985) provide measurements of ultragiant CCN in both marine and continental environments. Johnson (1982) discusses some of the differences between the role of ultragiant nuclei in continental and maritime clouds. Ochs and Semonin (1979) demonstrated that the presence of these CCN in their mass-conserving parcel model, which included both accretion and stochastic collision–coalescence (Ochs and Yao 1978; Ochs 1978), significantly accelerated the development of precipitation. Johnson (1982) showed that a simple Bowen-type (1950) continuous collection model (Johnson 1979) and a fully stochastic model (Young 1975) produced large raindrops and similar radar reflectivities in nearly identical times when ultragiant nuclei were included in the initial spectra. Caylor and Illingworth (1987) and Illingworth (1988) argued that high differential radar reflectivity in the upper parts of warm precipitating cumuli over the United Kingdom and Arizona indicated the presence of low concentrations of very large raindrops and were consistent with a model of drop growth by collection of cloud water on ultragiant CCN.

Beard et al. (1986) and Johnson et al. (1986) suggested that even very large raindrops (D > 4 mm) can grow from ultragiant nuclei by accretion of cloud water alone during a single up–down trajectory through idealized shallow cumuli with steady updrafts and subadia-

Unauthenticated | Downloaded 12/05/22 11:56 AM UTC

batic liquid water contents. However, their calculations suffered from a number of simplifying assumptions. In their model (D. B. Johnson 1998, personal communication), drops with terminal velocities matching a constant updraft speed were inserted at cloud top and allowed to grow by coalescence as they fell to the ground. The authors did not consider any possible limitations to the time available for the growth of raindrop embryos on the way up through the cloud, did not model the lateral movement or drops into and out of the updraft, and assumed a constant updraft speed throughout the depth of the cloud. In real clouds, updrafts and cloud liquid water (CLW) evolve rapidly, and raindrop trajectories are influenced by horizontal flow, which can carry them into and out of favorable growth regions. These limitations were recognized by Rauber et al. (1991), who argued that large drop recirculation may be required to keep raindrops in favorable growth regimes for a sufficient time.

In this paper, the third of this series, we revisit Woodcock's (1952) and Johnson's (1982) hypothesis that accretion of cloud water on ultragiant CCN can explain the growth of raindrops in warm convective clouds. The hypothesized role of the ultragiant nuclei is to produce the initial tail of large droplets capable of initiating coalescence at the early stages in the life cycle of a cloud. Our goal is to determine the range of conditions under which drops can grow by accretion of cloud water alone from ultragiant CCN to observed raindrop sizes during simple up–down trajectories through Hawaiian clouds. The formation and evolution of rain in these clouds was documented by Szumowski et al. (1997, 1998b; hereafter Part I and Part II) using dual-Doppler radar and aircraft data. Our approach is to use a Lagrangian drop-growth trajectory model applied within dual-Doppler-derived four-dimensional kinematic fields. These fields provide realistic timescales and magnitudes of convective updrafts and additionally take into account horizontal flow variations that can transport drops into and out of updrafts. The temporal evolution of the observed kinematic fields provides a strong constraint on the time available for rain to form and provides a much more realistic test than in earlier studies. In section 2, we describe the radar analyses and their limitations, and the model structure and parameterizations. In section 3, we discuss the results of the drop-growth calculations in a rainband that occurred on 10 August during the Hawaiian Rainband Project (HaRP). In section 4, we summarize our findings based on 10 August and other simulations.

2. Methodology

The radar data used to derive the kinematic fields used by the trajectory model were collected by the CP3 and CP4 National Center for Atmospheric Research (NCAR) 5-cm wavelength Doppler radars. A detailed description of the radar analysis domain, the sampling procedures, and the analysis methods appears in Part I. The 3D kinematic fields were synthesized at 300-m horizontal and 200-m vertical resolution every 2.5 min. One 5-min gap occurred on 10 August due to the scanning procedures (see Part I). A 15 × 15 km domain, encompassing an evolving high reflectivity core, was used for each set of trajectory calculations. The sizes and positions of drops along their trajectories were compared to the evolving radar reflectivity fields.

The model microphysics were limited to the simple continuous collection equation

$$\frac{dM_i}{dt} = \frac{\pi}{4}(D_i + d)^2 E(D_i, d)\chi(x, y, z, t)\rho_a[\upsilon(D_i) - \upsilon(d)], \tag{1}$$

where M_i is the mass of the drop; D_i and d are the equivalent spherical diameters of large and small drops, respectively; $\upsilon(D_i)$ and $\upsilon(d)$ are their respective terminal velocities; χ is the cloud liquid water mixing ratio; $E(D_i, d)$ is collection efficiency; and ρ_a is the density of air. Traditionally (e.g., Johnson 1982) terms d and $\upsilon(d)$ have been neglected as insignificant in the growth equation. These terms were retained in the model growth equation after tests indicated that they could have a substantial effect on drop-growth trajectories and final drop size. The terminal velocities of the falling drops in the trajectory model were formulated after Rogers and Yau (1989). In terms of drop diameter, Eq. (1) becomes

$$\frac{dD_i}{dt} = \frac{(D_i + d)^2}{D_i^2}\frac{\rho_a}{2\rho_L}E(D_i, d)\chi(x, y, z, t)[\upsilon(D_i) - \upsilon(d)], \tag{2}$$

where ρ_L is the density of water.

Two versions of the model (forward and backward in time) were developed to calculate drop trajectories. In both cases, the 3D gridded kinematic fields were interpolated to the location of each drop at every time step using first-order in time and second-order in space schemes. A second-order-accurate predictor–corrector scheme was used to calculate drop trajectories and growth. A 10-s time step was chosen based on the grid resolution and the maximum vector velocities of the raindrops. During each time step, the drops grew by accretion of cloud water; were transported by the interpolated, radar-derived kinematic motions; and fell at their terminal velocities. The accuracy of the predictor–corrector scheme was tested using combined forward–backward calculations for several drops. In all 30-min simulations (15-min trajectories forward and back) the displacement of the drops from their original position was less than 5 m and the departure from their original size was less than 0.05 μm. Decreasing the time step to 5 s resulted in no significant change in model accuracy, confirming that the 10-s time step was sufficiently small.

In the forward model, drops were released from var-

Unauthenticated | Downloaded 12/05/22 11:56 AM UTC

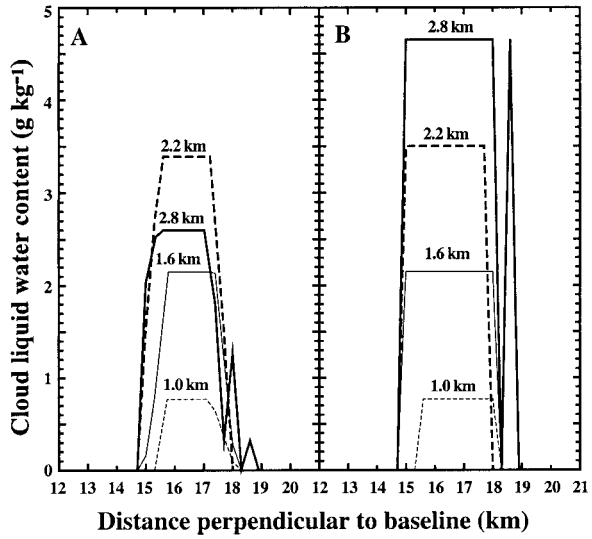

FIG. 2. Example of the parameterized horizontal distribution of CLW across the 10 Aug updraft. The CLW content is plotted at four elevations and, in the prescribed profile, is a function of the updraft intensity.

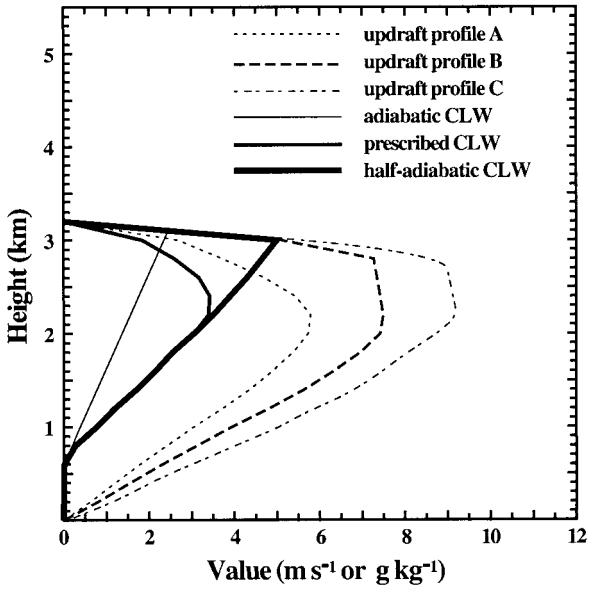

FIG. 3. Vertical profiles of the CLW content and the updraft in the center of the updraft core. Profiles are plotted at the times of peak updraft speeds. All the profiles used in the sensitivity runs are shown.

ious parts of the cloud at different times in the early stages of cells' life cycles. Typically 500 to 1200 drops were released on a plane of constant elevation enclosing the main updraft region. The backward runs were designed to determine the source regions of large raindrops present within the observed high-reflectivity cores during the mature rain shaft stage (see Parts I and II). The backward trajectories were also used to estimate maximum possible raindrop sizes for single up–down trajectories under given conditions. In the backward calculation, if the updraft speed at drop's location never exceeded the drop's terminal velocity by the time the drop reached the cloud top, the trajectory was terminated and the drop was rejected as too large. Only those drops whose terminal velocities eventually became less than the updraft speed were able to complete the backward traverse through the cloud. The release plane for the backward calculations encompassed the high reflectivity regions and was generally chosen near the cloud-base level.

Model limitations and sensitivity tests

Four factors that influence the results of the trajectory model calculations were studied: 1) the horizontal and vertical distribution of the CLW content; 2) the collection efficiencies between cloud droplets and growing collector drops; 3) the true vertical motions in the clouds, which are likely to be underestimated due to radar processing procedures; and 4) the size and position of the drops at the time of release.

1) CLOUD LIQUID WATER CONTENT

Three parameterizations of CLW content were used in the model simulations: half-adiabatic, prescribed, and adiabatic. The adiabatic values were determined from aircraft soundings using a parcel ascent from the mixed layer typically present in the lowest few hundred meters above the ocean surface. The prescribed liquid water

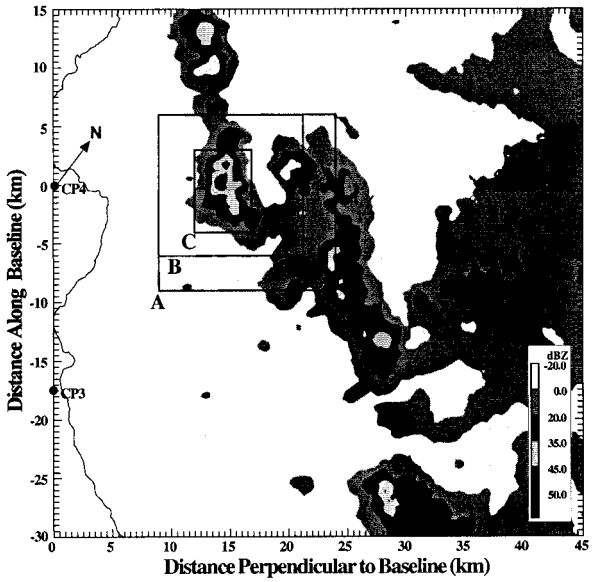

FIG. 4. Horizontal cross section of the radar reflectivity field at 1.2 km on 10 Aug 1990. Box A depicts the location of the subdomain used for the trajectory calculations. Boxes B and C are the subsets of this domain used in later figures. Box C corresponds to panels shown in Figs. 6, 7, 9, 11, and 13.

Unauthenticated | Downloaded 12/05/22 11:56 AM UTC

TABLE 1. Summary of 10 Aug 1990 sets of backward-run sensitivity tests.

	Control	1	2	3	4	5	6	7	8	9	10
Collection efficiency	Semiempirical						Unity				
CLW[a]	pre	½ ad	pre	pre	ad	ad	½ ad	pre	pre	pre	ad
Updraft profile (Fig. 3)	B	B	A	C	A	B	B	A	B	C	B
D_{max} (mm)[b]	5.0	4.0	3.5	6.0	4.0	5.5	5.5	6.0	7.0	8.0	8.5
D_{min} (μm)[c]	70	130	60	80	50	40	70	40	50	60	20

[a] pre = prescribed, ad = adiabatic (see Fig. 3).
[b] D_{max} is the diameter of the largest drop that completed a backward trajectory.
[c] D_{min} is the smallest diameter to which raindrops with release diameters of 4 mm (3 mm for sets 1 and 2) shrank in the backward calculations.

content represents what we believe is a close estimate of the actual three-dimensional distribution of CLW. Aircraft penetrations of updraft cores (Part II) showed a typical bell-shaped structure of the CLW content, with maximum values in the region of the strongest updraft, and values decreasing to zero near the updraft edges. The vertical profiles of CLW content within the strongest updrafts were near-adiabatic in the lower parts of the clouds and closer to half-adiabatic near cloud top.

For the prescribed CLW content, the "core updraft" was defined at any elevation as that part of an updraft where $(w_m - 1.5 \text{ m s}^{-1}) < w \leq w_m$, where w is the updraft speed and w_m is the maximum updraft value observed at that elevation. The CLW was assumed to be adiabatic within the core below an arbitrary altitude Z_0. The height Z_0 was chosen to be one to two grid points below the level of the radar-derived cell peak updraft in each of the synthesized volumes, typically just above the midpoint between cloud base and cloud top (e.g., 2.0 km on 10 August). The CLW was decreased from its adiabatic value to zero between Z_0 and the cloud top (Z_T) within the updraft core. Outside the updraft core, the CLW was a function of w. The cloud liquid water content l is given by

$$l = l_a f_1(w) f_2(z), \tag{3}$$

where $f_1(w)$ is

$$f_1(w) = 1 \quad \text{for } (w_m - 1.5 \text{ m s}^{-1}) < w \leq w_m,$$

$$f_1(w) = \sin\left[\frac{\pi w}{2(w_m - 1.5)}\right] \quad \text{for } 0 \leq w \leq (w_m - 1.5 \text{ m s}^{-1}),$$

$$f_1(w) = 0 \quad \text{for } w < 0,$$

and $f_2(z)$ is

$$f_2(z) = 1 \quad \text{for } z < Z_0,$$

$$f_2(z) = [\exp(Z_0 - z)]\left\{\tan\left[\frac{\pi(z - Z_0)}{4}\right]\right\} \quad \text{for } Z_0 \leq z < Z_T,$$

$$f_2(z) = 0 \quad \text{for } z \geq Z_T,$$

where l_a is the adiabatic liquid water content. This parameterization accounts for the effects of dry air entrainment at cloud top and mixing at the cloud edges. Examples of the spatial distribution of CLW content from 10 August 1990 radar volumes are illustrated in Figs. 2 and 3. The peak value of the prescribed cloud liquid water in any synthesized volume was ~3.4 g kg^{-1}.

In sensitivity tests, half-adiabatic or adiabatic profiles were also used. In both cases, the liquid water content was assigned its half-adiabatic or adiabatic value at all grid points where $w > 0$. In all simulations, the cloud liquid water was evenly partitioned among a monodisperse cloud droplet population, which was assumed to have a droplet concentration of 150 cm^{-3}, a value typical of observations (see Part II). The diameter of the monodisperse droplets ranged from a few microns near cloud edges (e.g., 5.7 μm at 0.1 g kg^{-1} CLW) to a maximum of 16.8, 18.7, and 21.2 μm in the upper part of the updraft core in the half-adiabatic, control, and adiabatic runs, respectively.

2) COLLECTION EFFICIENCY

Model collection efficiencies for drops growing by accretion were extrapolated from semiempirical values provided by Beard and Ochs (1984). They showed that collection efficiencies for 100- to 1000-μm collector drops range from near 0% to about 70% for cloud droplet diameters of 2 to 32 μm. In the trajectory model these laboratory data were extrapolated for collector drops smaller than 100 μm and larger than 1 mm since reliable experimental data were not available for those sizes. Unity efficiencies have often been used to calculate drop growth by sweep-out of cloud water in simple collection models (e.g., Bowen 1950) since there is a large degree of uncertainty associated with collection efficiencies for various drop size combinations. Test calculations with unity collection efficiencies were performed to determine the upper limit of drop growth rates.

3) UPDRAFT INTENSITY

A detailed description of the derivation of the vertical motion field from the synthesized dual-Doppler radial

Unauthenticated | Downloaded 12/05/22 11:56 AM UTC

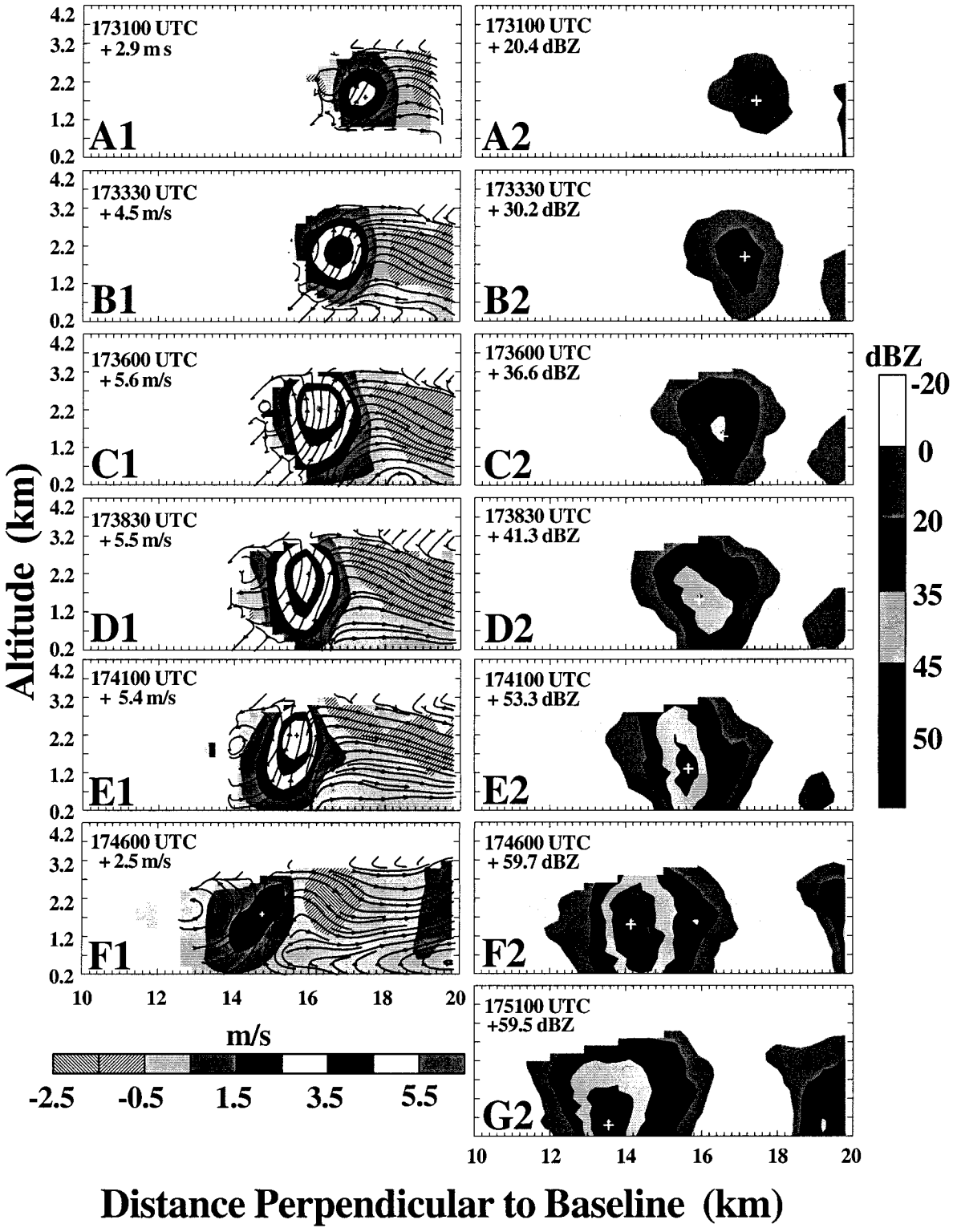

FIG. 5. Evolution of the convective updraft and the most intense high reflectivity core embedded in the 10 Aug rainband; (a1)–(f1) show the evolution of the vertical motion field with overlaid streamlines; (a2)–(g2) show the corresponding reflectivity cross sections. Radar reflectivity values are interpolated. The peak range-gate reflectivity observed at 1746 UTC was 61.9 dBZ.

Unauthenticated | Downloaded 12/05/22 11:56 AM UTC

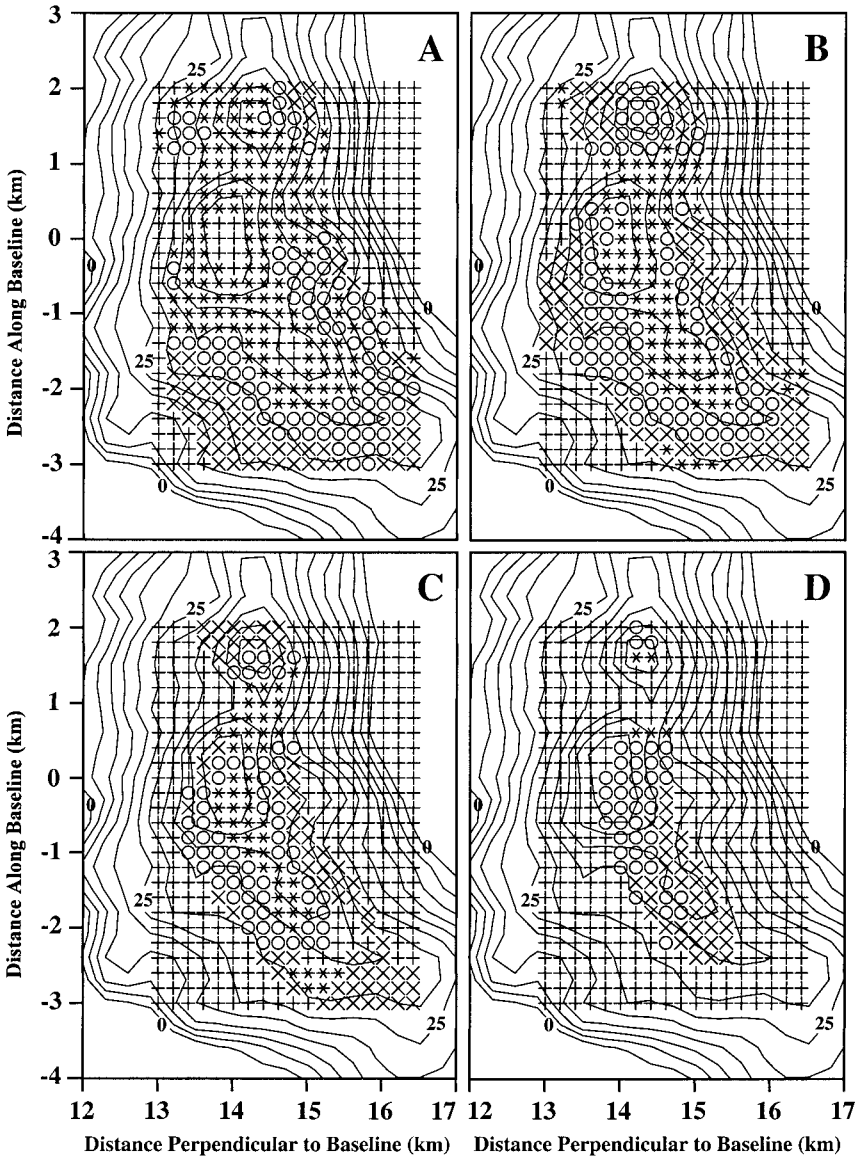

FIG. 6. Initial size reached at $t = 0$ by an array of drops released for control runs at $t = 1050$ s at an elevation of 0.6 km in the most intense part of the rainband on 10 Aug 1990; (a)–(d) final drop sizes of 1, 2, 3, and 4 mm, respectively. The following notation depicts the size at $t = 0$: $\times = D < 100$ μm, $\bigcirc = 100$–200 μm, $* = 200$–400 μm, $+ = D > 400$ μm.

velocities appears in Part I. We argued in Part I that the updrafts, particularly near cloud top, were underestimated due to the averaging procedures and integration methods used in dual-Doppler syntheses. The radar-derived peak updraft on 10 August was 5.6 m s^{-1}. The value of maximum possible updraft speed, based on the convective available potential energy (CAPE) from the sounding taken on 10 August, was 12.3 m s^{-1}. Peak updrafts of 10 m s^{-1} were observed by aircraft in convective cells with CAPE values similar to 10 August (Part II). The aircraft-measured updrafts maintained their intensity up to the equilibrium level. These characteristics of the vertical updraft structure were simulated by modifying the Doppler-derived vertical profiles and the intensity of the updrafts in some simulations. The updraft profiles used in 10 August simulations were A) unaltered, B) enhanced by 33%, and C) enhanced by 66% from the Doppler-derived values. The enhanced updrafts (B and C) were assumed to maintain their peak speed from the level of the Doppler-derived maximum (typically 2.2–2.4 km) to 0.4 km below the estimated cloud top. Within the 0.4-km-deep layer immediately below cloud top, the updraft magnitude was decreased from its peak speed to zero (Fig. 3). Aircraft data and

Unauthenticated | Downloaded 12/05/22 11:56 AM UTC

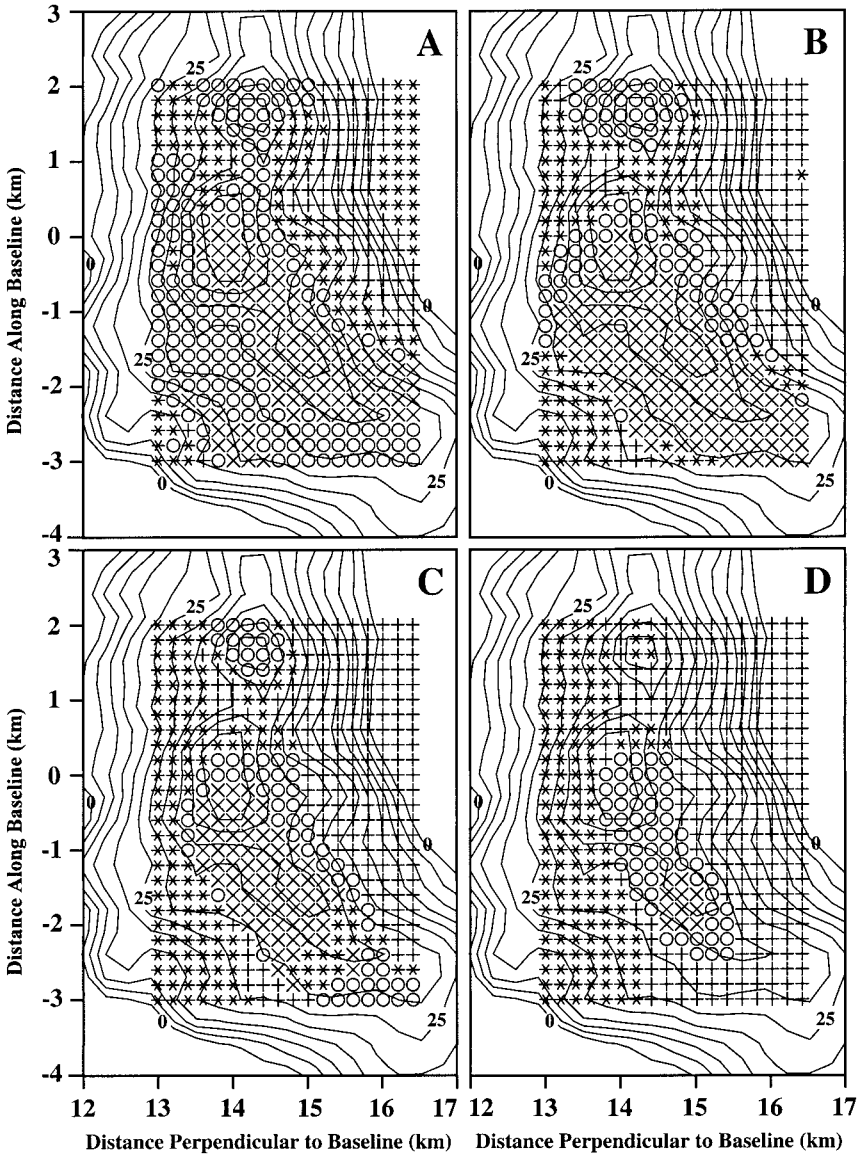

FIG. 7. Initial height reached at $t = 0$ by an array of drops released in control runs at $t = 1050$ s and the elevation of 0.6 km in the most intense part of the rainband on 10 Aug 1990; (a)–(d) final drop sizes of 1, 2, 3, and 4 mm, respectively. The following notation depicts drop height at $t = 0$: $\times = z < 1.0$ km, $\bigcirc = 1.0$–2.0 km, $* = 2.0$–3.0 km, $+ = z > 3.0$ km.

CAPE estimates suggest that updraft profile B best resembles the actual conditions found in the Hawaiian rainbands. The peak updraft in this profile was approximately an average of the Doppler-derived and CAPE-estimated peak updraft speeds.

A fundamental limitation of the radar data is that 3D kinematic motions can be retrieved through dual-Doppler syntheses only in regions where echoes have intensities above the noise background. During the earliest part of a cell's life cycle, when no precipitation-sized particles have yet formed, kinematic fields cannot be derived. It is obvious that an updraft must be present where a convective cloud begins to form, but the cloud cannot be detected until the particles composing it become sufficiently large. Even then, the derivation of vertical velocity remains inaccurate until larger droplets fill the entire depth of the cloud. A several-minute lag exists between the time when a convective updraft first forms and the time when the vertical motions can be accurately resolved by the Doppler radars. When analyzing the history of the early drop-growth trajectories (droplets that originated near cloud base in the initial stages of the updraft intensification), the assumption must be made that some cloud droplet growth has oc-

Unauthenticated | Downloaded 12/05/22 11:56 AM UTC

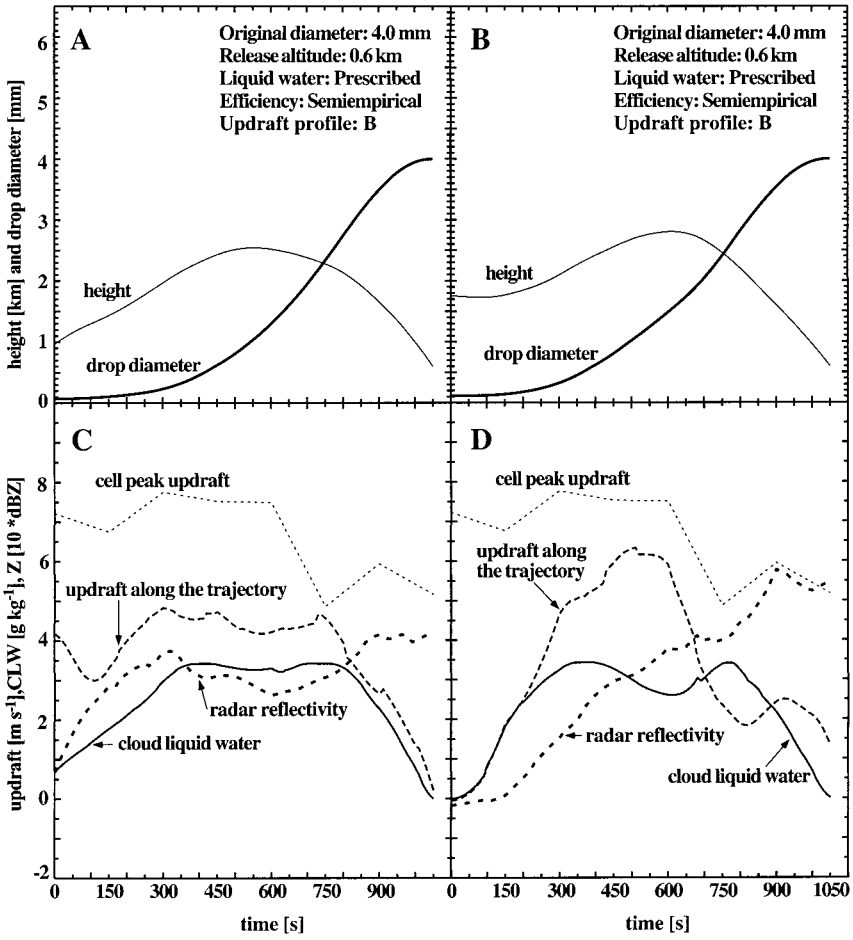

FIG. 8. Individual backward trajectories for 4-mm drops released in a control run at (a), (c) $x = 14.8$ km, $y = -1.6$ km and (b), (d) $x = 13.8$ km, $y = 0.0$ km. Panels (a) and (b) show drop size and height along the trajectory; (c), (d) show the updraft, CLW, and reflectivity experienced by the drops along their trajectories, as well as the peak updraft in the cell.

curred before the time when the vertical motions are first fully resolved.

4) DROP SIZE AND POSITION AT THE TIME OF RELEASE

The following terminology will be used for convenience. The term ''initial'' refers to the time of the first radar volume used in the calculation and will be used to describe drop parameters at the beginning of a forward run or at the end of a backward run. The term ''final'' refers to the latest time in a calculation and will be used to describe drop parameters at the end of a forward run or at the beginning of a backward run. ''Cloud droplets'' will refer to droplets with $D \leq 100$ μm; ''small drizzle drops,'' 100 μm $< D \leq 200$ μm; ''large drizzle,'' 200 μm $< D \leq 400$ μm; and ''small raindrops,'' 400 μm $< D \leq 1000$ μm. The term ''shrinking'' will be used to describe negative growth by accretion in the backward calculations. Each set of runs used a specific parameterization of CLW, collection efficiency, and updraft structure. Each run in a set consisted of an array of drops of a specific size released at a specific elevation. The set of ''control runs'' used conditions we believe most closely resemble those in nature, namely, the prescribed cloud liquid water parameterization, semiempirical collection efficiencies from Beard and Ochs (1984), and updraft profile B.

Backward runs were used to determine 1) the range of conditions under which raindrops completed backward trajectories and 2) the size and location of drops in the cloud at the time of the initial radar volume ($t = 0$). Raindrops with final sizes ranging from 1 to 8 mm were released in a plane near cloud base at $t = 1050$ and $z = 0.6$ km (box C of Fig. 4). The release plane encompassed the high-reflectivity cores shortly after the cells reached their peak intensities. Drop-growth rates were calculated for 11 sets of conditions (Table 1). The

Unauthenticated | Downloaded 12/05/22 11:56 AM UTC

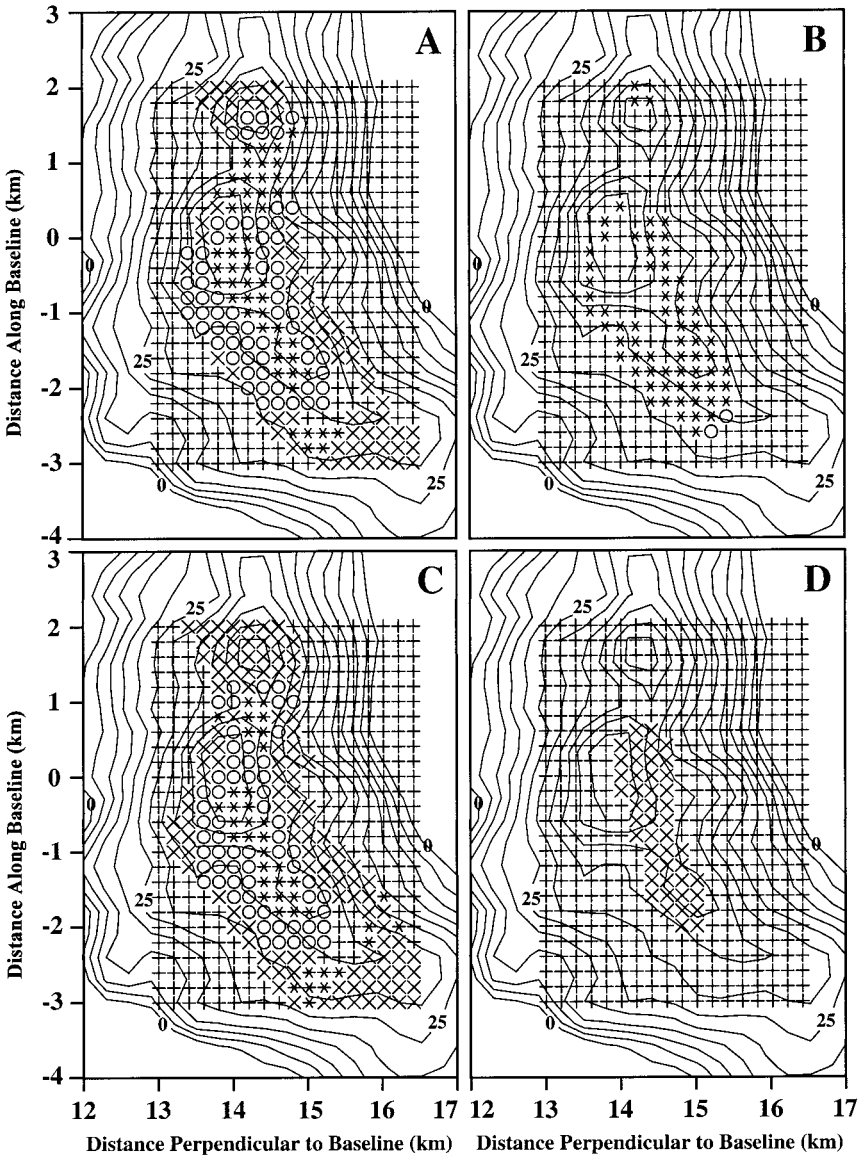

FIG. 9. Same as Fig. 6 except (a)–(c) show drop arrays for a release diameter of 3 mm for a control run, a run from set 1, and a run from set 5; (d) shows a 5-mm drop array from a run in set 5. Table 1 lists the conditions used in each set.

set of control runs will be used as the base for comparisons between the simulations.

In the forward simulations drops with initial diameters ranging from 40 to 100 μm were released in planes encompassing the updraft at $t = 0$. The release planes were located between cloud base (~630 m) and the middle of the cloud. The initial sizes were based on Woodcock's (1953) measurements shown in Fig. 1. The concentrations of deliquesced salt particles just below cloud base (99% relative humidity) measured by Woodcock in Hawaiian clouds ranged from 10^4 m^{-3} for particles >20-μm diameter to 1 m^{-3} for particles >100-μm diameter. Many measurements of sea salt aerosol size distributions have been reported since Woodcock's data appeared (e.g., Meszaros and Vissy 1974; de Leeuw 1986; O'Dowd et al. 1997). These measurements also show the characteristic dependence on wind speed. O'Dowd et al. (1997), for example, reported concentrations of sea salt aerosol at 80% relative humidity ranging from 10^4 to 10^3 m^{-3} for particles >20-μm diameter and wind speeds ranging from 17 to 9 m s^{-1}, respectively. All of these studies reported particles with diameters >100 μm. Ingested into an updraft, these ultragiant particles can serve immediately as coalescence nuclei. The drops that were released higher in the cloud were released with larger sizes to account for growth during the assumed ascent between cloud base and the release altitude. The release time varied from t

Unauthenticated | Downloaded 12/05/22 11:56 AM UTC

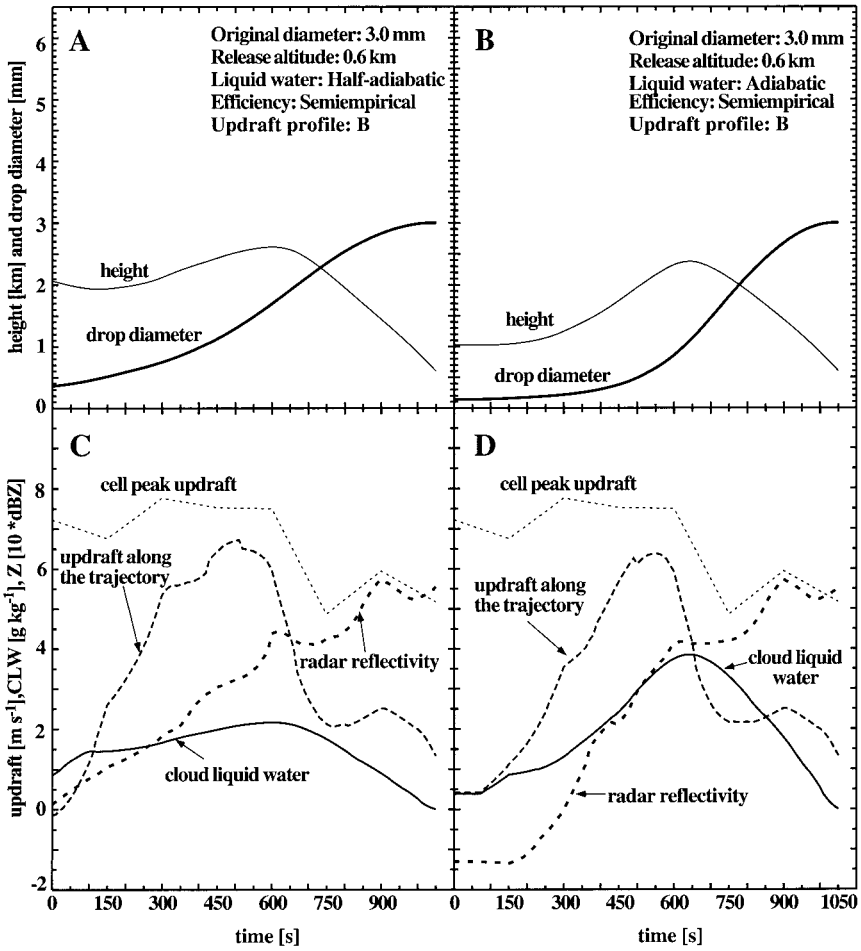

FIG. 10. Same as Fig. 8 except for 3-mm drops released at $x = 13.8$ km, $y = 0.0$ km for conditions from (a), (c) set 1 and (b), (d) set 5.

$= 0$ to $t = 150$ s after the time of the first radar volume used in the simulation.

3. Results of the trajectory calculations

Simulations were carried out for rainbands that occurred on 10 and 22 August 1990. The evolution of the rainbands on each of these days was described in detail in Part I. In this paper we focus on the results from 10 August because the life cycles of two cells containing high-reflectivity cores were captured by the Doppler radars from the first echo through dissipation. This case provided the most complete kinematic data for the drop-growth and trajectory calculations. Trajectory calculations were also performed for 22 August because this rainband developed the highest reflectivity observed in the project, had strong well-defined updrafts, and developed a reflectivity maximum located close to the cloud top (see Part I). The primary deficiency of the 22 August case was that radar data were unavailable early in the lifetime of the cells. At the time of the first radar volume, the two updraft cores associated with the developing rain shafts were already near their peak intensity. Because of the missing data, only partial backward trajectories for the drops arriving in the high reflectivity cores could be calculated. The results from 22 August generally support the conclusions derived from the 10 August simulations. Details of the 22 August simulations can be found in Szumowski (1997).

Two rainbands developed on the morning of 10 August (Fig. 4). This study concentrates on the portion of the shoreward rainband enclosed by Box A in Fig. 4. Two high reflectivity cores developed within this region of the rainband. The evolution of the radar reflectivity and the vertical motion field for the more intense core are shown in Fig. 5. The rain shaft reached a peak reflectivity of 61.9 dBZ at 1.6 km (Fig. 5f2), 15 min after the initial echo was detected (Fig. 5a2), and maintained high (>50 dBZ) reflectivity for over 10 min (Figs. 5e2–5g2). It is evident from Figs. 5a1 and 5b1 that the convective updraft associated with this rain shaft was not fully resolved until precipitation reached the ground (Fig. 5c1).

In the backward calculations, the drops shrink as they

Unauthenticated | Downloaded 12/05/22 11:56 AM UTC

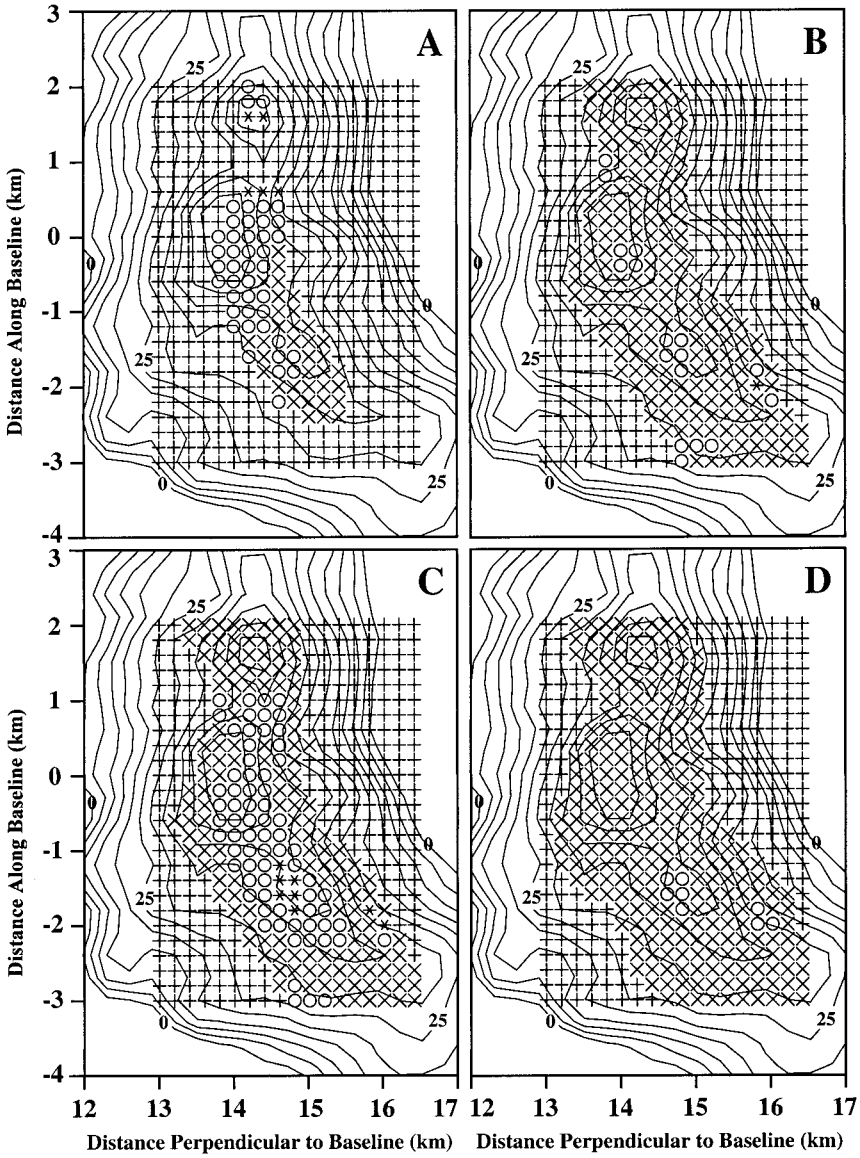

FIG. 11. Same as Fig. 6 except (a)–(d) show the initial size of 4-mm drop arrays released in a control run and runs from sets 8, 9, and 10, respectively (see Table 1).

ascend and then descend to their point of origin at the initial time. Each drop's ascent rate in the backward trajectory is controlled by the difference between its terminal velocity and the updraft at the location of the drop. The larger the drop or the weaker the updraft, the faster the ascent rate. Therefore, drops that are small or that experience a strong updraft near the final time of their trajectories tend to remain in the lower part of the cloud. Drops that experience a weak updraft near the final time and stronger updraft near the initial time traverse nearly the entire depth of the cloud. The updraft profile experienced by a drop along its trajectory controls the altitude to which each drop rises and therefore the mean drop-shrinking rate for the entire trajectory. Since cloud liquid water content throughout most of the cloud depth increases with height, drops that reach higher altitudes during their trajectories have larger mean shrinking rates than drops that follow ''flat'' trajectories.

a. The backward control runs

Figures 6a–d and 7a–d show the initial ($t = 0$) size and height, respectively, of 1-, 2-, 3-, and 4-mm drops as a function of their final position for the control run set. Figure 6 shows that the greatest shrinking in the array of small (1 mm) raindrops generally occurred for those released near the edges of the high reflectivity region. The greatest shrinking in the array of large (4

Unauthenticated | Downloaded 12/05/22 11:56 AM UTC

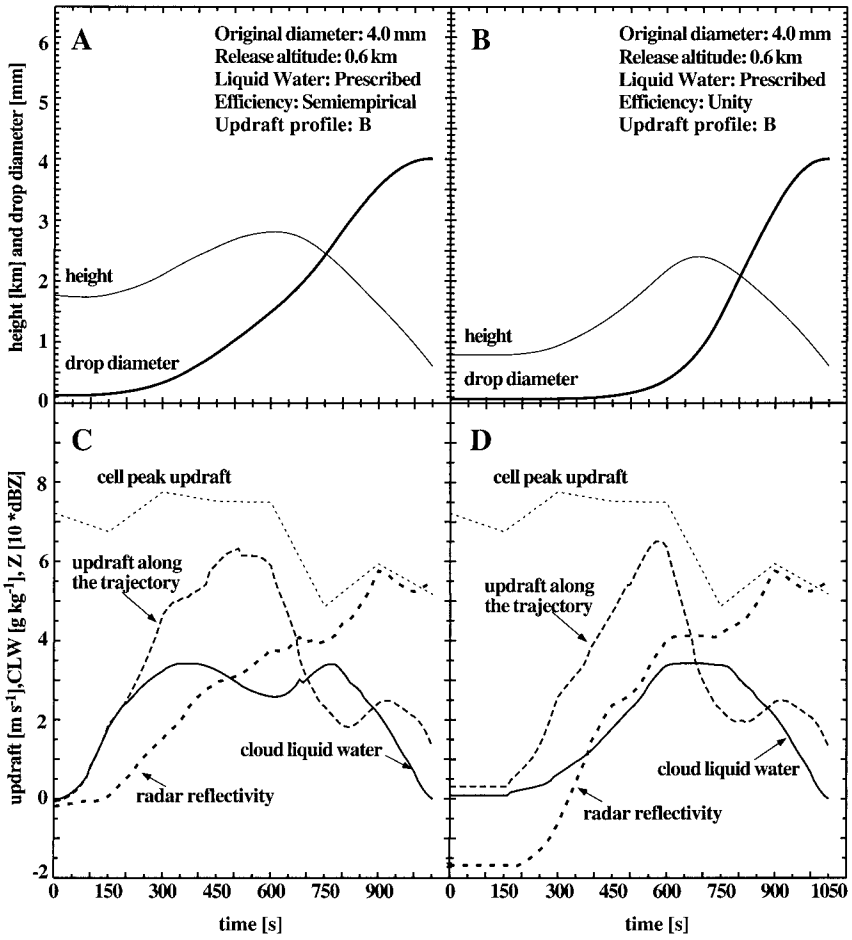

FIG. 12. Same as Fig. 8 except for 4-mm drops released at $x = 13.8$ km and $y = 0.0$ km in (a), (c) a control run and (b), (d) a run from set 8.

mm) raindrops generally occurred for those released along the axis of high reflectivity. Figure 7 indicates that most of the drops that shrank to small drizzle or cloud droplet sizes originated in the lower part of the cloud between 1000 and 2000 m at $t = 0$. All "*" and "+" drops positioned near the edges of the release plane in Fig. 7 exited the kinematic field through the side of the rainband and through cloud top, and therefore represent unrealistic trajectories.

The top panels of Fig. 8 show examples of growth histories along trajectories in a height–time plane for two 4-mm drops. The bottom panels show cloud parameters along the trajectories. The first drop, located at $x = 14.8$ km, $y = -1.6$ km (Figs. 8a,c), was released in an area with radar reflectivity of 40 to 45 dBZ. The drop remained in a nearly steady 4 to 5 m s^{-1} updraft through the middle half of its trajectory. This updraft history allowed the drop to rise to $\approx$2.7 km and to remain in the high (>3 g kg^{-1}) CLW content over a period of more than 10 min. The drop shrank to $D \approx 75$ μm. The second drop (Figs. 8b,d) was released farther to the north, at $x = 13.8$ km, $y = 0.0$ km, within the high reflectivity core. It followed a similar trajectory, experiencing a slightly weaker updraft near the release time and a stronger 5 to 6 m s^{-1} updraft in the middle part of the trajectory. The drop reached an altitude of nearly 3 km, where the CLW content was reduced to account for cloud-top entrainment (note the dip in the CLW plot near $t = 500$ s). This drop had descended only to about 1.7 km at $t = 0$ since during the downward traverse through the cloud it entered a region of unreliable kinematic data, as indicated by a sharp decrease in updraft, reflectivity, and CLW between 0 and 150 s. This is an example of the impact on early trajectory calculations of the radars' inability to depict an updraft in the early stages of cloud development. The drop shown in Fig. 8b shrank to a small drizzle drop ($D \approx 160$ μm) at $t = 0$. Although it was still located high in the cloud, the radar echo was too weak to derive reliable vertical motions from the dual-Doppler synthesis procedures.

The results of the backward trajectory calculations

Unauthenticated | Downloaded 12/05/22 11:56 AM UTC

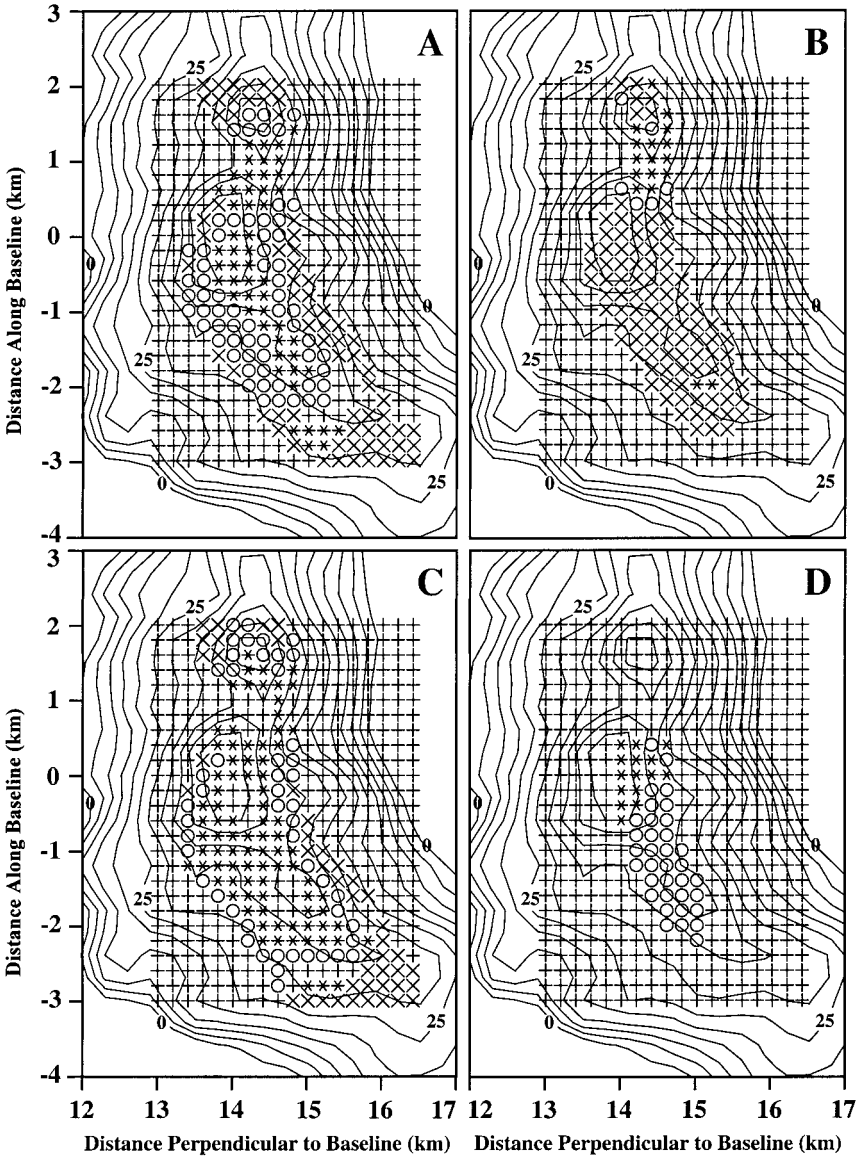

FIG. 13. Same as Fig. 6 except (a)–(c) show the initial size of 3-mm drop arrays for a control run, a run from set 2, and a run from set 3; (d) shows a 5-mm release array for a run from set 5 (see Table 1).

for the control runs illustrate that (in forward thinking) large raindrops can grow by accretion in realistic timescales from large cloud droplets and small drizzle drops present within the initial updraft. The trajectories of the largest raindrops arrived at the final time in a region closely corresponding to the interior of the 40-dBZ contour, especially in the southern part of the release plane. Trajectories of smaller (1 and 2 mm) raindrops, which originated as cloud droplets at the initial time, arrived closer to the edges of the rainband, near the 20- and 30-dBZ contours. The calculations imply that a collection of cloud droplets or small drizzle drops released at various elevations within the cloud at $t = 0$ can end up as 1-mm drops on the edges of the high reflectivity region and 4-mm drops along the center axis of the high reflectivity region. The simulations place the largest drops at the location of the highest reflectivities and smaller drops at the location of weaker reflectivities. The results also imply that, at the specific time and elevation of the release plane, it is unlikely to find realistic backward trajectories for 1- or 2-mm drops that originate within the high reflectivity region. In the control runs all drops larger than 5 mm exited through the top of the cloud. If the parameters of the control runs are in close agreement with reality, then the growth of drops larger than 5 mm that were present near cloud base within this

Unauthenticated | Downloaded 12/05/22 11:56 AM UTC

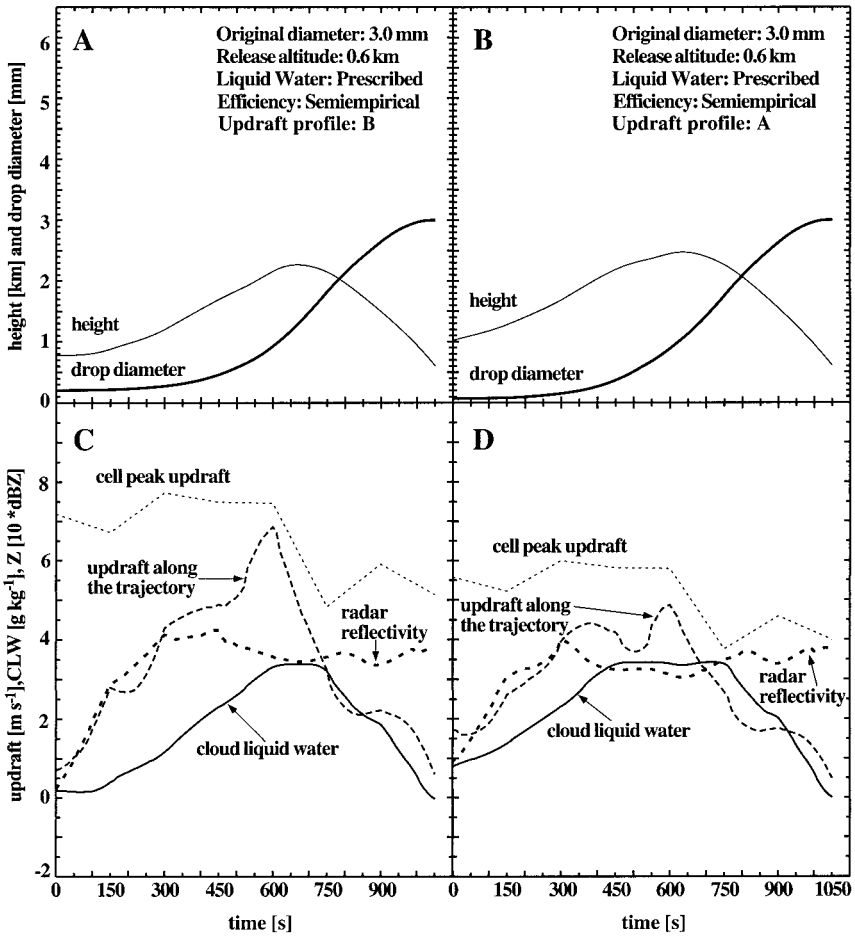

FIG. 14. Same as Fig. 8 except for 3-mm drops released at $x = 14.6$ km and $y = -1.4$ km in (a), (c) a control run and (b), (d) a run from set 2.

section of the rainband must have involved other processes, such as large hydrometeor self-collection or recirculation.

b. Sensitivity tests

The sensitivity of drop-growth rates to three parameters (CLW distribution, collection efficiencies, and updraft profile) is examined in this section. The analyses of the sensitivity tests focus on the differences between the set of control runs (shown in Figs. 6–8) and sets of runs with other conditions as listed in Table 1. For all backward runs discussed in this section, the release plane was at the same location and time as the plane depicted in Fig. 6.

1) CLOUD LIQUID WATER CONTENT

Figure 9 shows the release position and initial size of 3-mm drops for a run from the control set (Fig. 9a), set 1 (Fig. 9b), and set 5 (Fig. 9c) (see Table 1). Figure 9d depicts a 5-mm drop release plane for set 5. All three sets used semiempirical collection efficiencies and updraft profile B but varied in CLW from half-adiabatic (Fig. 9b), to prescribed (Fig. 9a), to adiabatic (Figs. 9c,d). The half-adiabatic run produced no cloud droplets at $t = 0$. Most of the 3-mm drops that completed their backward trajectories in this run shrank to sizes between 200 and 400 μm at $t = 0$, but not to cloud droplets. Very few of these drops were located below 2 km at $t = 0$. The terminal velocities of most drops at $t = 0$ were on the order of 1 to 2 m s^{-1}, exceeding the magnitude of the weak updraft present near the initial time. This was especially true for drops released in the northern section of the release plane. As expected, drops shrank most rapidly in the adiabatic runs, with a large number of drops shrinking to cloud droplets. These drops were located near the edges of the high reflectivity region when the release size was 3 mm (Fig. 9c) and along the axis of high reflectivity when the release size was 5 mm (Fig. 9d).

Single trajectories for 3-mm drops released from the

Unauthenticated | Downloaded 12/05/22 11:56 AM UTC

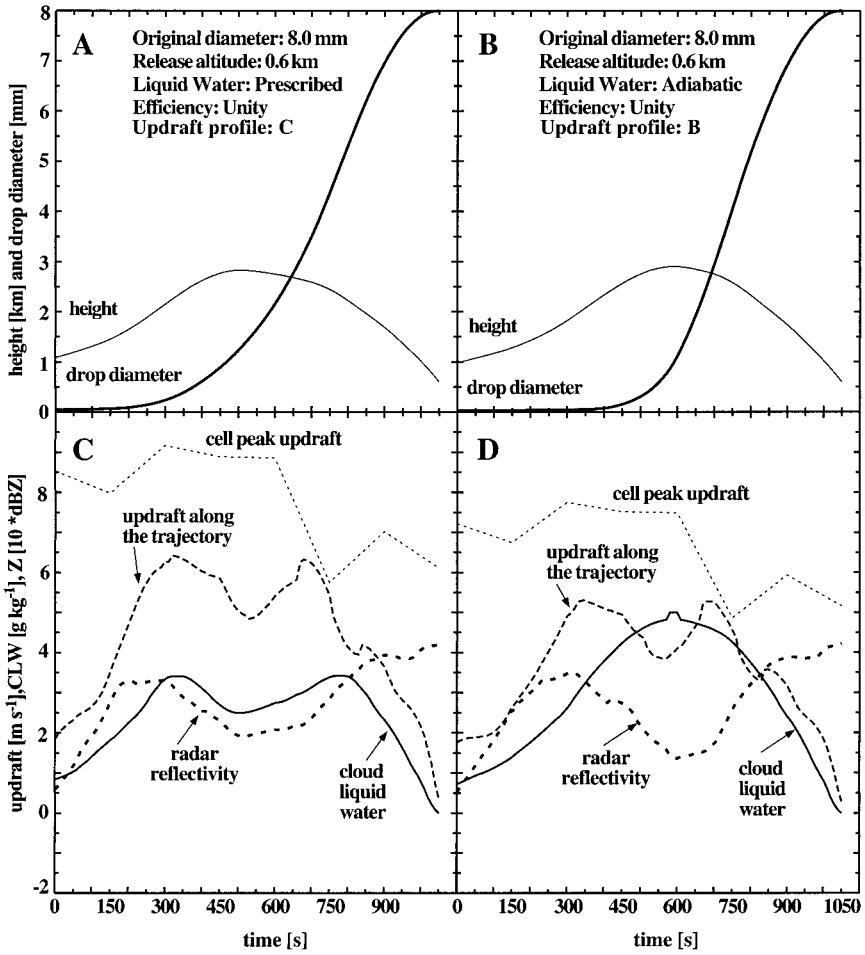

FIG. 15. Same as Fig. 8 except for 8-mm drops released at $x = 14.6$ km and $y = -1.4$ km for conditions from (a), (c) set 9 and (b), (d) set 10.

same positions within the high reflectivity core in each of the three runs were examined. Figure 10 compares the half-adiabatic run with the adiabatic run for a drop released at $x = 13.8$ km, $y = 0.0$ km. The control run trajectory is not shown in Fig. 10 because it was very similar to the trajectory from the adiabatic run. The close resemblance between the control and adiabatic runs implies that the drop in the control run remained in an adiabatic region of the updraft core. The drop in the half-adiabatic run (Figs. 10a,c) remained in the upper part of the cloud, while in the adiabatic run (Figs. 10b,d) the drop shrank more rapidly, resulting in a faster descent rate as t approached 0. For drops at other locations, there were significant differences between the control and adiabatic runs. Some drops that exited through cloud top in the control run shrank sufficiently in the adiabatic run to complete up–down trajectories. In the adiabatic runs all drops that traversed through the cloud at altitudes higher than 2.5 km encountered CLW contents greater than 4 g kg^{-1}, a value that is probably unrealistically high for shallow Hawaiian clouds (see Part II).

2) COLLECTION EFFICIENCY

Two sets of collection efficiencies were used: semiempirical values based on Beard and Ochs (1984) and unity efficiencies. In Fig. 11, the difference between a control run with 4-mm drops (Fig. 11a) and a simulation with similar conditions except for unity efficiencies (set 8, Fig. 11b) is quite striking. Nearly all 4-mm raindrops released anywhere within the 25-dBZ contour area shrank to cloud droplets at $t = 0$ when unity collection efficiencies were used.

The difference in shrinking rate between unity and semiempirical collection efficiencies for two 4-mm drops released at $x = 13.8$ km, $y = 0.0$ km is demonstrated in Fig. 12. In the unity collection efficiency run (Figs. 12b,d) the shrinking rate for the drop increased dramatically between 600 and 1000 s during the drop's near suspension and ascent (corresponding to fall in forward space) within the high CLW content. Although the cumulative CLW encountered by this drop along its trajectory was much smaller than for the drop

Unauthenticated | Downloaded 12/05/22 11:56 AM UTC

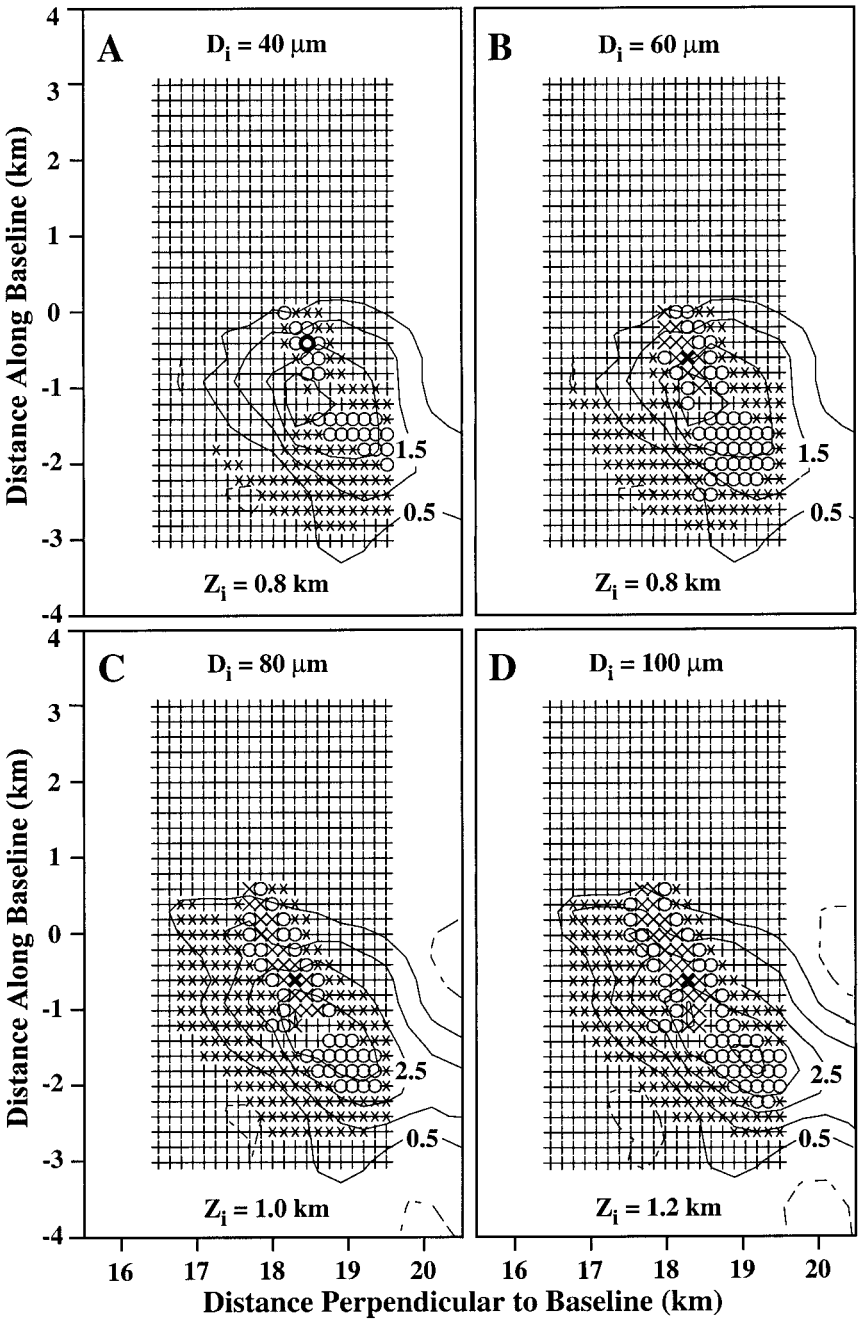

FIG. 16. Release planes for cloud droplets in the forward control run at $t = 0$: (a) 40-μm droplets released at 0.8 km, (b) 60-μm droplets released at 0.8 km, (c) 80-μm droplets released at 1.0 km, and (d) 100-μm droplets released at 1.2 km. The following symbols have been used to depict the final drop size at $t = 1050$ s: $\times = D > 3$ mm, $\bigcirc$ = 2–3 mm, * = 1–2 mm, + = $D < 1$ mm. The bold markers indicate the release positions of individual drops shown in Fig. 17.

in the control run (Figs. 12a,c), the unity collection efficiencies for the drop in Figs. 12b,d more than offset the effect of reduced cloud water. With unity efficiencies, the drop shrank from a 4-mm drop to a cloud droplet in about 10 min. In the control run, the raindrop reached a higher altitude and had a longer residence time in the high CLW content. It shrank to a 120-μm drizzle drop high in the cloud at 1.8 km at $t = 0$, at which time the updraft was only partially resolved by the radar because precipitation-sized particles had not yet formed in that section of the rainband. Because of its position high in the cloud at $t = 0$, this drop had

Unauthenticated | Downloaded 12/05/22 11:56 AM UTC

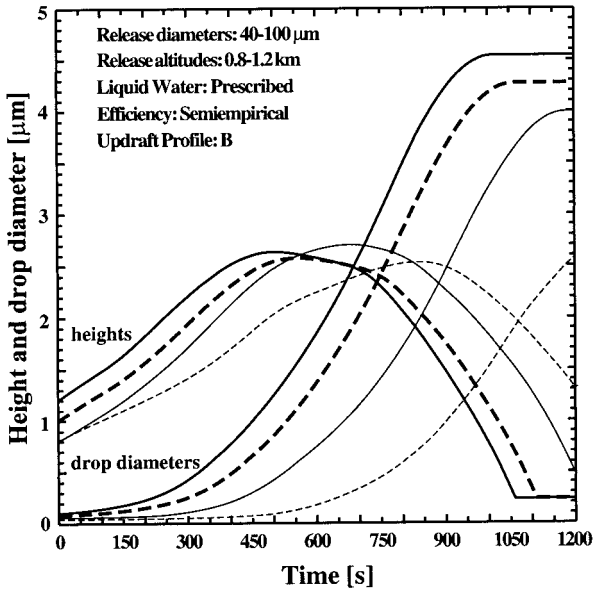

FIG. 17. Drop size and altitude along the trajectory for four drops released at locations highlighted in Fig. 16. Thin dashed lines are for a 40-μm drop released at 0.8 km (release plane shown in Fig. 16a), thin solid lines for a 60-μm drop released at 0.8 km (Fig. 16b), thick dashed for a 80-μm drop released at 1.0 km (Fig. 16c), and thick solid for a 100-μm drop released at 1.2 km (Fig. 16d).

potential for significant shrinking prior to $t = 0$ during the initial development of the cloud when an updraft could not be resolved.

Modifying set 8 by incorporating an adiabatic CLW profile (set 10) slightly broadened the area where 4-mm raindrops shrunk to cloud droplet sizes, but did not have a pronounced effect on the overall growth rate of the drops (e.g., Fig. 11d). Modifying set 8 by enhancing the updraft (set 9) had a *negative* effect on the overall drop growth rate for the 4-mm drops (e.g., Fig. 11c). This sensitivity to the updraft intensity and its vertical profile is discussed below.

3) UPDRAFT INTENSITY

Figures 13a–c show, respectively, the initial droplet size as a function of release position for 3-mm drops released in a run from the control set, a run from set 2 (which used updraft profile A), and a run from set 3 (which used updraft profile C). Figure 13d shows the results for 5-mm drops released in a run from set 3.

Most of the 3-mm drops that completed backward trajectories in the run with updraft profile A shrank to cloud droplets at $t = 0$. In contrast, fewer 3-mm drops shrank to cloud droplets in the control run, which had a stronger updraft. However, some 4-mm drops shrank to cloud and drizzle drops in the control run (Fig. 6d), while all 4-mm drops followed unrealistic trajectories in the run with updraft profile A, exiting through cloud top. The behavior of the 3-mm drops is contrary to the intuitive assumption that a stronger updraft should promote a greater shrinking rate due to the updraft's ability to suspend larger raindrops. The reason for this behavior is evident in Fig. 14, which compares trajectories of two drops released at the same position ($x = 14.6$ km, $y = -1.4$ km) for the control run (Figs. 14a,c) and the run with updraft profile A (Figs. 14b,d). In forward thinking, a weak updraft late in a drop's trajectory will allow it to fall faster to cloud base. In the backward trajectory the drop ascends faster toward cloud top. A weaker updraft during the time period from 700 to 1000 s in the run with updraft profile A promoted the drop's ascent to a higher altitude. Reaching a higher altitude resulted in 1) a longer residence time of the drop in a high CLW environment, 2) a later arrival back at cloud base, and 3) a greater mean shrinking rate. In the run with updraft profile C, the trajectories were even flatter and the drop residence time in high CLW regions was even shorter. As shown in Fig. 13c, none of the 3-mm drops released within the high reflectivity region shrank to a cloud droplet size. However, the drops released in weaker reflectivity traversed through a weaker mean updraft and were able to shrink to cloud droplet sizes. The 5-mm drops released in high reflectivity regions in the run with updraft profile C (Fig. 13d) followed trajectories more favorable for shrinking but were still unable to shrink to cloud droplet sizes at $t = 0$. Once again, this appeared to be related to the inability to derive reliable vertical motions from dual-Doppler synthesis procedures between $t = 0$ and 150 s.

Drops with equivalent spherical diameters as large as 8 mm have been observed in Hawaiian rainbands (Beard et al. 1986; Part II). In our simulations, 8-mm raindrops shrank to cloud droplets only in the extreme conditions of sets 9 and 10. Trajectories for two 8-mm drops released at $x = 14.6$ km, $y = -1.4$ km using 9 and 10 conditions are shown in Fig. 15. For the drop in the run from set 10, the shrinking rate was so extreme that the 8-mm drop became a cloud droplet in less than 10 min. This growth rate appears to be too rapid when compared with the time evolution of the cell containing the high reflectivity core on 10 August 1990 (see Fig. 5). If conditions such as adiabatic CLW and near-unity collection efficiency occurred in nature, raindrops would rapidly grow to 4- to 8-mm diameters anywhere in a rainband where a convective updraft of a few meters per second was present.

The results of the backward sensitivity tests for 10 August 1990 are summarized in Table 1. For each set of runs, Table 1 lists the diameter of the largest drop that completed a backward trajectory without exiting through cloud top. The table also shows the minimum diameter that any 4-mm drop (3 mm for sets 1 and 2) achieved at $t = 0$. In all simulations, some of the raindrops with $D \geq 3$ mm shrank to cloud droplets ($D < 100$ μm) at $t = 0$. In all sets except 1 and 2, some raindrops with $D \geq 4$ mm completed backward trajectories becoming cloud droplets. Many others shrank to small drizzle drops.

Unauthenticated | Downloaded 12/05/22 11:56 AM UTC

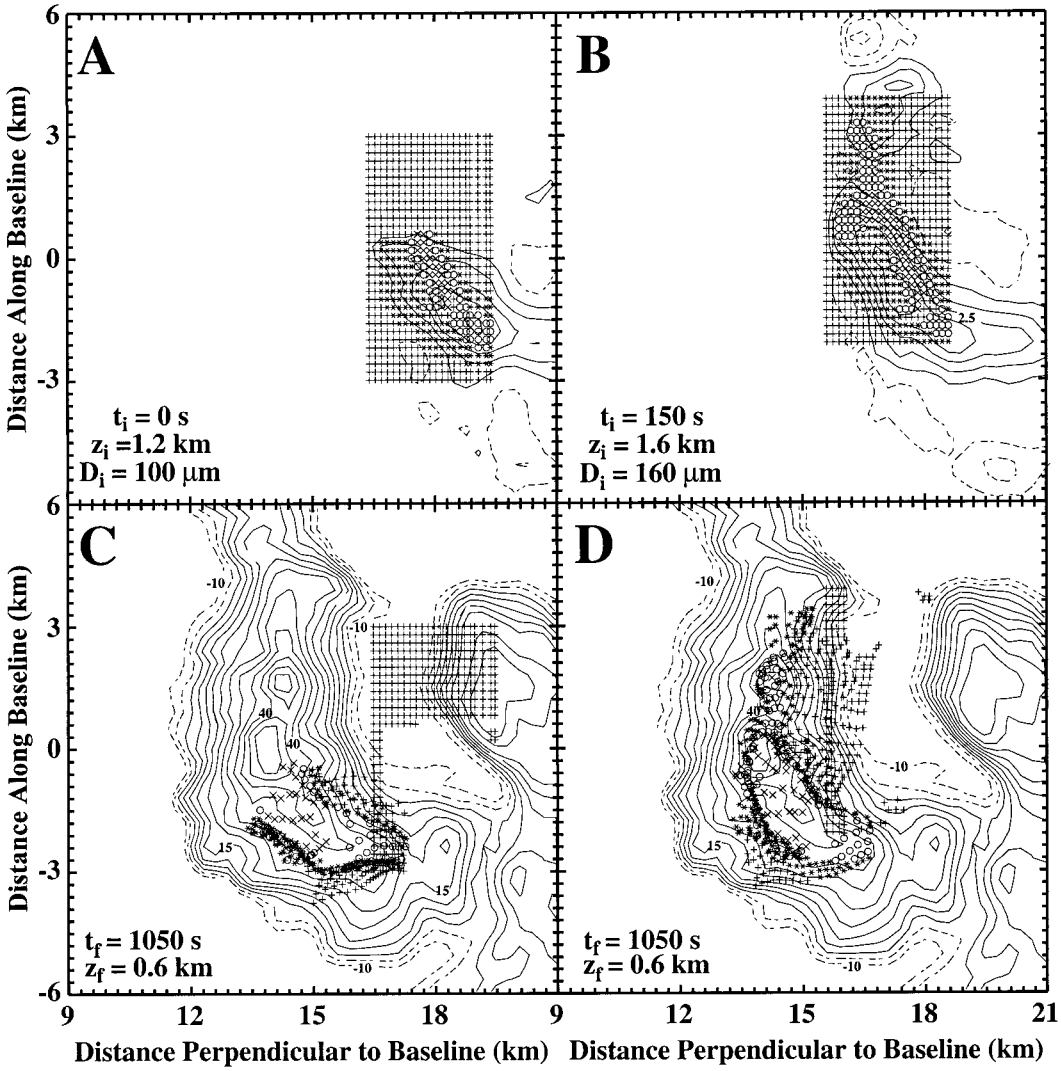

FIG. 18. Forward-run release plane overlaid over the vertical motion contours at (a) $t = 0$ s and 1.2 km for an array of 100-μm drops, (b) $t = 150$ s and 1.6 km for an array of 160 μm; (c) and (d) show the final size and position of raindrops at $t = 1050$ s overlaid over the reflectivity field at 0.6 km, for drops released in (a) and (b), respectively.

c. The forward simulations

Figures 16a–d show the release planes for 40-, 60-, 80-, and 100-μm droplets at 0.8, 0.8, 1.0, and 1.2 km, respectively. The vertical motion field at the level of the release planes is also shown in each panel. The 60- to 100-μm droplets that were released on the upwind side of the northern part of the updraft at $t = 0$ grew to the largest sizes ($D > 3$ mm, Figs. 16b–d). The 40-μm droplets released just upwind of the updraft core on its north and south sides grew to raindrops with diameters between 2 and 3 mm. Growth histories of the individual drops (bold in Fig. 16) released in the northern part of the updraft are shown in Fig. 17. All drops grew to sizes between 0.8 and 1.1 mm during the ascent and reached peak altitudes between 2.5 and 2.7 km. Drops with similar sizes were observed during aircraft penetrations near cloud top in Hawaiian rainbands (see Part II). The most rapid growth occurred in the suspension period near the cloud summit and the subsequent descent through the cloud, which is consistent with the evolution of the reflectivity fields and the observations of raindrop spectra presented in Parts I and II. Increasing the release size from 40 to 60 μm had the greatest effect on the overall growth of the drops.

Figure 18 shows that the area of radar-resolved vertical motion only covered part of the release plane at $t = 0$. Cloud droplets within the data-void region were unable to initiate trajectories (see Fig. 18c). Figure 18c shows that all of the drops fell out in the southern part of the rainband. The backward runs showed that raindrops re-

Unauthenticated | Downloaded 12/05/22 11:56 AM UTC

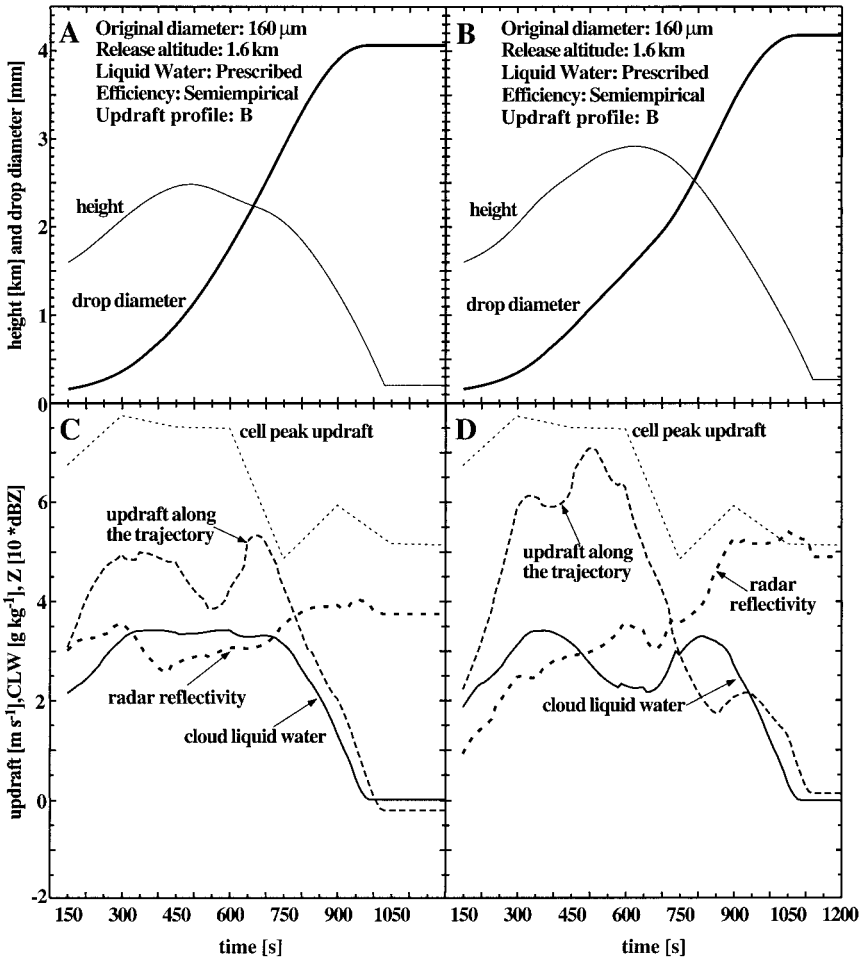

FIG. 19. Same as Fig. 4.6 except for two 160-μm drops released at $x = 17.4$ km, $y = -0.3$ km; and $x = 16.8$ km, $y = 1.2$ km at $t = 150$ s and $z = 1.6$ km in the forward control runs.

leased in the northern part of the rainband encountered the data-void region near $t = 0$, preventing them from shrinking further to cloud droplets. A simple exercise was performed in the forward runs to address the problem of the updraft not being resolved by the radars at $t = 0$ in the northern part of the rainband. First, we assumed that an updraft was present in this region at $t = 0$. We then used the typical growth history of a 100-μm drop in the southern part of the rainband (e.g., Fig. 17) to determine the size and elevation of the drop at 150 s. The drop shown in Fig. 17 reached a size of approximately 160 μm at an altitude of about 1.6 km. This altitude and size was used to define a new release plane of 160-μm drops at $t = 150$ s, as shown in Fig. 18b. At this time, the northern updraft was well resolved. Most of these drops fell out of cloud base ~15 min later. Figure 18d shows that many raindrops with $D > 2$ mm landed in the high reflectivity region, with the largest drops centered along the axis of highest reflectivities. Figures 18c,d exhibit the interesting feature of trajectory ''size sorting.'' The regions where the largest drops landed were often characterized by the absence of smaller raindrops, most of which fell on the edges of high reflectivities. This spatial distribution of large and small raindrops in the trajectory calculations may be related to the transport of smaller drops out of the core of the updraft by the outflow near the inversion level. This ''fountaining'' mechanism was suggested by radar and aircraft observations reported in Part II.

Two sample drop trajectories from the forward control run with 160-μm release diameter are shown in Fig. 19. The first drop (Figs. 19a,c) experienced an extended suspension period in a 5 m s^{-1} updraft and 3 g kg^{-1} CLW content during which most of its growth occurred. The drop fell out of cloud base in ~40-dBZ reflectivity, having grown to $D = 4.1$ mm in approximately 16 min. The second drop experienced a stronger updraft near $t = 500$ s, which raised the drop closer to cloud top (~3.0 km). The dip in CLW content along the trajectory near $t = 500$ s reflects the fact that the prescribed CLW content was decreased near cloud top to account for dry air entrainment (see Fig. 3). Despite the noticeable de-

Unauthenticated | Downloaded 12/05/22 11:56 AM UTC

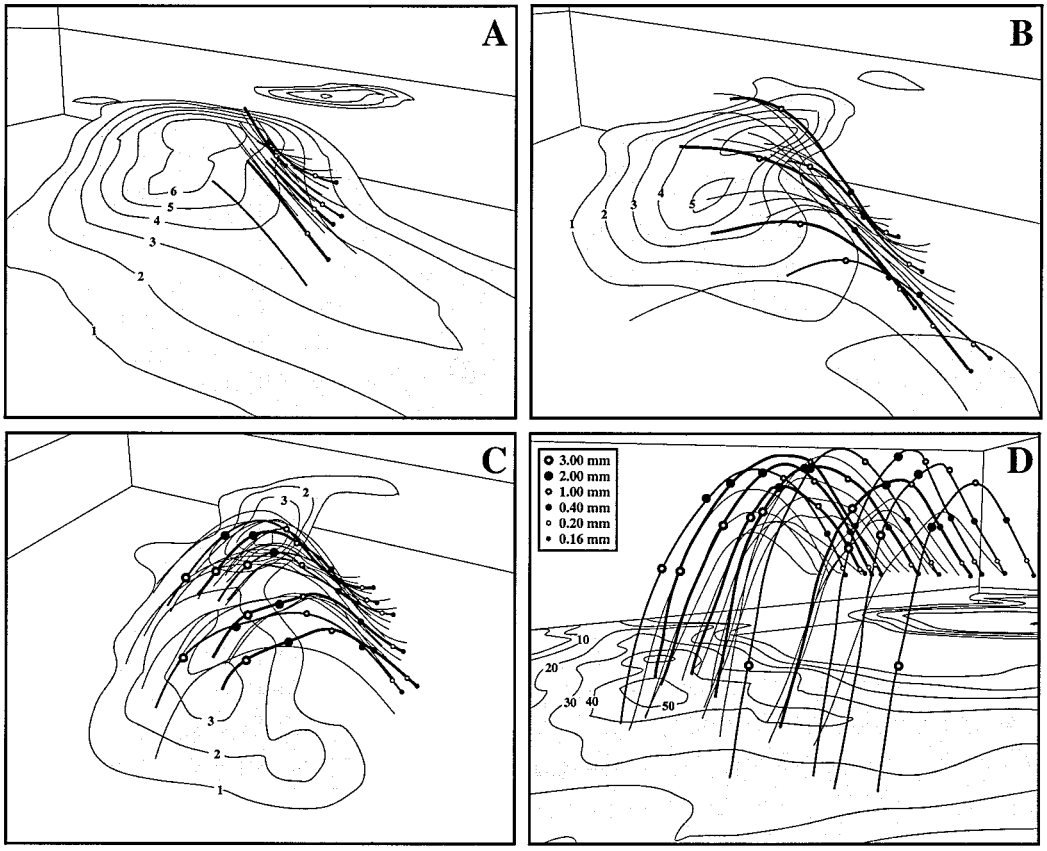

FIG. 20. Favorable trajectories for raindrop growth in the forward control run on 10 Aug 1990. (a) Trajectories on the upwind side of the updraft through 300 s, and updraft at 2.0 km and 300 s; (b) trajectories through 600 s (during the near-suspension period), and updraft at 2.6 km at 600 s; (c) trajectories through 900 s, and the updraft at 2.0 km and 900 s; (d) trajectories through 1050 s, and a cross section of the radar reflectivity field at 0.6 km and 1050 s. Markers indicate the position at which drops on selected trajectories reached the sizes given in the legend in (d).

crease in CLW content the second drop grew to 4.2 mm and fell out of cloud base within the high reflectivity core (~55 dBZ) in about 18 min.

4. Summary

The results of the trajectory model calculations in the simulated cloud environment using the Doppler-derived kinematic fields showed that accretion of cloud water on giant and ultragiant nuclei can account for the formation of rain in observed timescales. Raindrops with sizes of 1–4 mm formed regularly and fell within the 10 August rainband over the entire range of tested conditions. Based on laboratory measurements and observations, the control runs are believed to most closely represent the conditions occurring in nature. In the control runs, drops as large as 5 mm formed on cloud droplets with sizes comparable to the deliquesced sea salt particles observed by Woodcock (1953) in concentrations of ~10 to 10^3 m^{-3} (Fig. 1). Several raindrops with diameters >5 mm were sampled within the high reflectivity cores embedded in the rainbands. For cloud droplets to grow to these exceptionally large sizes in observed timescales, one of the following conditions must be met: 1) the drops must encounter CLW higher than prescribed, 2) the collection efficiencies must be higher than the semiempirical values used in the model, 3) random self-collection or binary breakup (e.g., Reisin et al. 1998) must occur, or 4) a recirculation process must be involved in the growth of a few drops.

The control runs illustrate that 1- to 5-mm raindrops can grow by accretion in 15–20 min. The general tendency noticed in all forward and backward simulations was for the largest drops to fall within regions of radar reflectivity greater than 35 dBZ, and for the smaller drops to fall in parts of the rainband with weaker reflectivity. This size sorting is consistent with the observations reported in Part II. We also showed in Part II that the larger drops, present only within the high reflectivity core, had a low probability of collisional breakup because of low concentrations of smaller raindrops. The growth rates and trajectories of 1- to 5-mm raindrops agreed remarkably well with the observed evolution of the reflectivity field. The most rapid rate

Unauthenticated | Downloaded 12/05/22 11:56 AM UTC

of growth in the model occurred during a near-suspension period near cloud top and during the early fall through the upper parts of the cloud. This results is in good agreement with the sharp reflectivity gradients observed near cloud top by the radars (Part I), and the observations of Takahashi (1981) and Takahashi et al. (1989).

Sensitivity tests were performed over the range of conditions listed in Table 1. In these tests, raindrops as large as 3.5–8.5 mm formed from cloud droplets. Sensitivity tests focused on three parameters: collection efficiencies, cloud liquid water distribution, and updraft intensity. Two limiting collection efficiencies, semiempirical and unity, were used in the sensitivity tests. Increasing the collection efficiencies from semiempirical to unity generally produced large increases in overall drop growth. The maximum size of raindrops increased from 5 to 7 mm when the efficiencies were increased. The 15–20-min time period required for shrinking to cloud and small drizzle drops in the control run was qualitatively consistent with the time period required for the development of the high reflectivity core from initial echo (Fig. 5). In contrast, shrinking rates for runs using unity collection efficiencies appeared unrealistically high. The suspension times for all unity collection efficiency runs were much shorter than for semiempirical collection efficiencies since the drops with unity collection efficiencies shrank much faster. The model calculations support the use of the semiempirical laboratory-based collection efficiencies. However, these collection efficiencies are based on measurements made at approximately 1000 mb (Beard and Ochs 1984). Recent measurements of coalescence efficiencies for small precipitation drops collecting other precipitation drops (Liu 1997) show that coalescence efficiencies increase at lower pressures due to reduced air film drainage between colliding drops. Although there are no similar data for accretion, drop-growth rates may be accelerated in the upper part of the cloud due to this effect. Additional laboratory data for accretion at reduced temperatures and pressures are needed to reduce the uncertainties in the drop-growth calculations.

The increase in the overall drop growth between the half-adiabatic and adiabatic CLW content cases was nearly the same as between runs with semiempirical and unity collection efficiencies. In the CLW sensitivity tests, the overall drop-growth rates decreased more by changing the CLW profile from prescribed to half-adiabatic than from prescribed to adiabatic. Raindrops as large as 2.5 mm grew from cloud droplets in the half-adiabatic case, while drops as large as 4.5 mm formed in the prescribed (control run) conditions. The largest drop sizes only increased by 0.5 to 1.0 mm between the prescribed and adiabatic conditions. The adiabatic and prescribed CLW content profiles differed near the edges and in the upper third of the updraft (Figs. 2 and 3). The final sizes of drops whose trajectories passed through those regions differed most between the simulations. Based on aircraft observations (Part II), the adiabatic conditions likely overestimated the CLW in the upper parts of the clouds. When drops reached altitudes above 2.5 km, the shrinking rates in the adiabatic CLW environment were extremely rapid.

The sensitivity of drop growth to the updraft profile was more complicated. The trajectory of a drop through the cloud is largely determined by the balance between the drop's terminal velocity and the intensity of the updraft along its trajectory. The effect of changes in the updraft profile on the overall shrinking of the drops in the backward runs depended on the release size of the drops. For example, updraft profile A provided the most favorable conditions for shrinking of 3-mm drops, while updraft profile C provided the most favorable conditions for shrinking 5-mm drops. In any updraft, there were trajectories that favored rapid growth. The most favorable trajectories in terms of the evolution of the updraft intensity and its vertical profile were identified as those in which 1) drops slowly rose in a moderate updraft to cloud-top levels on the edge of the updraft core, 2) entered into and remained in the strongest updraft during the suspension period and early fall through the upper part of the cloud, and 3) fell through the lower part of the cloud in a weakening updraft. Figure 20 shows three-dimensional views of such trajectories for droplets originating in the release plane shown in Fig. 18b. The drops that grew to the largest sizes in this and other forward runs rose on the upwind side of the updraft (Fig. 20a), reached their suspension period in the strong updraft (Fig. 20b), and fell in the center of the weakening updraft (Fig. 20c), contributing to the observed high reflectivity near cloud-base level (Fig. 20d).

Results of the trajectory calculations must be viewed with a clear understanding of the limitations of this study. The cloud liquid water content was not available from radar measurements and was parameterized based on our best understanding of the observed fields. The radar-derived updraft profiles, which generally underestimate the updraft speed in the upper parts of the clouds, were modified in some tests to conform to the magnitudes observed by the aircraft and the profiles expected from buoyancy analyses of the aircraft soundings. The radars were not capable of resolving the kinematic fields in the earliest stages of cloud development when no precipitation particles had yet formed, making it impossible, in some situations, to start the calculations with cloud droplets released at cloud base. This issue was addressed by assuming that an updraft was present in regions where it was detected by the radars several minutes later, and releasing droplets at a higher altitude with larger initial sizes.

5. Conclusions

The radar and aircraft data analyses presented in Parts I and II, combined with trajectory model calculations presented in this paper, provide a consistent and simple

Unauthenticated | Downloaded 12/05/22 11:56 AM UTC

explanation of warm rain formation. The model drop-growth calculations support Woodcock's (1952) hypothesis that raindrops form on the large sea salt particles present in maritime environments, and Johnson's (1982) conclusion (reached based on calculations in idealized one-dimensional clouds) that ''big aerosol particles make big raindrops.'' Despite the time and space constraints placed on the results by the observed evolution of the updrafts, these calculations show that the process of rain formation in warm maritime convective clouds is simple and efficient, provided that giant and ultragiant CCN are present near cloud base. While more complex processes leading to drop spectra broadening, such as mixing, stochastic condensation, stochastic coalescence and breakup also occur in nature, they appear to be unnecessary to explain the rapid formation of rain in warm maritime convective clouds.

Acknowledgments. We thank everyone at NCAR who contributed to the Hawaiian Rainband Project data acquisition and processing. We thank Wojciech Grabowski (NCAR) for his contribution to the development of the trajectory model, L. J. Miller and Bill Anderson (NCAR) for their assistance with radar analyses, and David Wojtowicz (University of Illinois) for his assistance with 3D visualization. Computing time was provided by NCAR, which is sponsored by the National Science Foundation. This research was sponsored by the National Science Foundation under Grants NSF ATM 9223165, NSF ATM 9634660, and NSF ATM 9421735.

REFERENCES

Beard, K. V., and H. T. Ochs, 1984: Collection and coalescence efficiencies for accretion. *J. Geophys. Res.,* **89,** 7165–7169.

——, and ——, 1993: Warm-rain initiation: An overview of microphysical mechanisms. *J. Appl. Meteor.,* **32,** 608–625.

——, D. B. Johnson, and D. Baumgardner, 1986: Aircraft observations of large raindrops in warm, shallow, convective clouds. *Geophys. Res. Lett.,* **13,** 991–994.

Berry, E. X., and R. L. Reinhardt, 1974a: An analysis of cloud drop growth by collection: Part I. Double distributions. *J. Atmos. Sci.,* **31,** 1814–1824.

——, and ——, 1974b: An analysis of cloud drop growth by collection: Part II. Single initial distributions. *J. Atmos. Sci.,* **31,** 1825–1831.

——, and ——, 1974c: An analysis of cloud drop growth by collection: Part III. Accretion and self-collection. *J. Atmos. Sci.,* **31,** 2118–2126.

——, and ——, 1974d: An analysis of cloud drop growth by collection: Part IV. A new parameterization. *J. Atmos. Sci.,* **31,** 2127–2135.

Bowen, E. G., 1950: The formation of rain by coalescence. *Aust. J. Sci. Res.,* **A3,** 193–213.

Caylor, I. J., and A. J. Illingworth, 1987: Radar observations and modelling of warm rain initiation. *Quart. J. Roy. Meteor. Soc.,* **113,** 1171–1191.

de Leeuw, G., 1986: Vertical profiles of giant particles close above the sea surface. *Tellus,* **38B,** 51–61.

Gillespie, D. T., 1972: The stochastic coalescence model for cloud drop growth. *J. Atmos. Sci.,* **29,** 1496–1510.

——, 1975: Three models for the coalescence growth of cloud drops. *J. Atmos. Sci.,* **32,** 600–607.

Hindman, E. E., II, P. V. Hobbs, and L. F. Radke, 1977a: Airborne investigations of aerosol particles from a paper mill. *J. Air Pollut. Control Assoc.,* **27,** 224–229.

——, ——, and ——, 1977b: Cloud condensation nucleus size distributions and their effects on cloud droplet size distributions. *J. Atmos. Sci.,* **34,** 951–956.

Hobbs, P. V., L. F. Radke, and E. E. Hindman II, 1976: An integrated airborne particle-measuring facility and its preliminary use in atmospheric aerosol studies. *J. Aerosol Sci.,* **7,** 195–211.

——, D. A. Bowdle, and L. F. Radke, 1985: Particles in the lower troposphere over the high plains of the United States. Part I: Size distributions, elemental compositions, and morphologies. *J. Climate Appl. Meteor.,* **24,** 1344–1356.

Houghton, H. G., 1938: Problems connected with the condensation and precipitation processes in the atmosphere. *Bull. Amer. Meteor. Soc.,* **19,** 152–159.

Illingworth, A. J., 1988: The formation of rain in convective clouds. *Nature,* **336,** 754–756.

Johnson, D. B., 1976: Ultragiant urban aerosol particles. *Science,* **194,** 941–942.

——, 1979: The role of coalescence nuclei in warm rain initiation. Ph.D. dissertation, University of Chicago, 119 pp. [Available from the University of Chicago, 5801 South Ellis, Chicago, IL 60637.]

——, 1982: The role of giant and ultragiant aerosol particles in warm rain initiation. *J. Atmos. Sci.,* **39,** 448–460.

——, K. V. Beard, and D. Baumgardner, 1986: Airborne observations of raindrop distributions in Hawaiian clouds. Preprints, *Conf. on Cloud Physics,* Vol. 2, Snowmass, CO, Amer. Meteor. Soc., 48–51.

Liu, S., 1997: Laboratory measurements of the effects of air pressure on the coalescence between small precipitation drops. M.S. thesis, Dept. of Atmospheric Sciences, University of Illinois, 67 pp. [Available from Department of Atmospheric Science, University of Illinois, 105 S. Gregory St., Urbana, IL 61801.]

Meszaros, A., and K. Vissy, 1974: Concentration, size distribution, and chemical nature of atmospheric aerosol particles in remote ocean areas. *J. Aerosol Sci.,* **5,** 101–109.

Nelson, R. T., and N. R. Gokhale, 1968: Concentration of giant particles below cloud bases. Preprints, *First National Conf. on Weather Modification,* Albany, NY, Amer. Meteor. Soc., 89–98.

Ochs, H. T., III, 1978: Moment-conserving techniques for warm cloud microphysical computations. Part II: Model testing and results. *J. Atmos. Sci.,* **35,** 1959–1973.

——, and C. S. Yao, 1978: Moment-conserving techniques for warm cloud microphysical computations. Part I: Numerical techniques. *J. Atmos. Sci.,* **35,** 1947–1958.

——, and R. G. Semonin, 1979: Sensitivity of a cloud model to an urban environment. *J. Appl. Meteor.,* **18,** 1118–1129.

O'Dowd, C. D., M. H. Smith, I. E. Consterdine, and J. A. Lowe, 1997: Marine aerosol, sea salt, and the marine sulphur cycle: A short review. *Atmos. Environ.,* **31,** 73–80.

Rauber, R. M., K. V. Beard, and B. M. Andrews, 1991: A mechanism for giant raindrop formation in warm, shallow, convective clouds. *J. Atmos. Sci.,* **48,** 1791–1797.

Reisin, T. G., Y. Yin, Z. Levin, and S. Tzivion, 1998: Development of giant drops and high-reflectivity cores in Hawaiian clouds: Numerical simulations using a kinematic model with detailed microphysics. *Atmos. Res.,* **45,** 275–297.

Robertson, D., 1974: Monte Carlo simulations of drop growth by accretion. *J. Atmos. Sci.,* **31,** 1344–1350.

Rogers, R. R., and M. K. Yau, 1989: *A Short Course in Cloud Physics.* 3d ed. Pergamon, 293 pp.

Szumowski, M. J., 1997: Rain formation in shallow tropical convection. Ph.D. dissertation, University of Illinois, Urbana–Champaign, 171 pp. [Available from University Microfilms Inc., P. O. Box 1346, Ann Arbor, MI 48106.]

——, R. M. Rauber, H. T. Ochs III, and L. J. Miller, 1997: The

Unauthenticated | Downloaded 12/05/22 11:56 AM UTC

microphysical structure and evolution of Hawaiian rainband clouds. Part I: Radar observations of rainbands containing high reflectivity cores. *J. Atmos. Sci.,* **54,** 369–385.

——, W. W. Grabowski, and H. T. Ochs III, 1998a: Simple two-dimensional framework designed to test warm rain microphysical models. *Atmos. Res.,* **45,** 299–326.

——, R. M. Rauber, H. T. Ochs III, and K. V. Beard, 1998b: The microphysical structure and evolution of Hawaiian rainband clouds. Part II: Aircraft measurements within rainbands containing high reflectivity cores. *J. Atmos. Sci.,* **55,** 208–226.

Takahashi, T., 1981: Warm rain study in Hawaii—Rain initiation. *J. Atmos. Sci.,* **38,** 347–369.

——, K. Yoneyama, and Y. Tsubota, 1989: Rain duration in Hawaiian trade-wind rainbands—Aircraft observation. *J. Atmos. Sci.,* **46,** 937–955.

Telford, J. W., 1955: A new aspect of coalescence theory. *J. Meteor.,* **12,** 436–444.

Woodcock, A. H., 1952: Atmospheric salt particles and raindrops. *J. Meteor.,* **9,** 200–212.

——, 1953: Salt nuclei in marine air as a function of altitude and wind force. *J. Meteor.,* **10,** 362–371.

——, and D. C. Blanchard, 1955: Test of the salt-nuclei hypothesis of rain formation. *Tellus,* **7,** 437–448.

——, R. A. Duce, and J. L. Moyers, 1971: Salt particles and raindrops in Hawaii. *J. Atmos. Sci.,* **28,** 1252–1257.

Young, K. C., 1975: The evolution of drop spectra due to condensation, coalescence, and breakup. *J. Atmos. Sci.,* **32,** 965–973.

Unauthenticated | Downloaded 12/05/22 11:56 AM UTC